International Journal of Heat and Mass Transfer 260 (2026) 128449

Contents lists available at ScienceDirect

International Journal of Heat and Mass Transfer

journal homepage: www.elsevier.com/locate/ijhmt

Thermofluidic characterization of additively manufactured butterfly-shaped inserts for heat transfer enhancement in tubular heat exchangers

Luca Pagliarini [a,*], Umberto Neviani [b], Teresa Primo [c], Antonio Del Prete [c], Sara Rainieri [a]

[a] Department of Engineering and Architecture, University of Parma, Parco Area delle Scienze 181/A, Parma, Italy
[b] DE Department of Engineering, Università di Ferrara, Ferrara, Italy
[c] Department of Engineering Innovation, Università del Salento, Complesso Ecotekne—Edificio "Corpo O" - Via Per Monteroni, 73100, Lecce, Italy

ARTICLE INFO

Keywords:
Tubular heat exchangers
Additive manufacturing
Passive heat transfer enhancement
Butterfly-shaped inserts
Infrared thermography

ABSTRACT

Heat transfer enhancement in heat exchangers still represents a crucial target for industrial plants efficiency. Passive methods, such as turbulators, are usually preferred to active ones due to their intrinsic capability to operate on the fluid flow without any need for auxiliary power. Butterfly-shaped inserts stand as valuable solutions for tubular heat exchangers due to their high degree of induced turbulence. However, their potential for turbulent regimes has not been fully disclosed yet. In the present work, different geometries of swirled butterfly inserts, directly integrated into tubular samples via additive manufacturing, are investigated with the aim of providing a full characterization of their thermofluidic behavior in the range $4000 < Re < 14{,}000$. Steady-state tests are carried out by circulating water through the test section, heated by Joule effect. Pressure drops are monitored via liquid column gauges; inlet/outlet water temperature is measured by means of thermocouples, while the outer wall temperature is acquired via infrared thermography. The local and global Nusselt numbers Nu and $\overline{Nu}$ are estimated by analytically correcting the measured outer wall temperature distributions. The fitting loss coefficients K related to each butterfly insert geometry are additionally estimated by considering the introduced local pressure losses. Finally, the Nusselt number and friction factor deviations from the benchmark geometry (plain tube) are compared through performance evaluation plots, by also quantifying performance indexes η. The results highlighted that holes in the butterfly insert layout are highly beneficial in terms of augmented heat transfer and mitigated pressure drops. The provided pieces of data can be useful for the design of butterfly-shaped inserts operating in turbulent flows, as well as for the conceptualization of novel heat transfer augmentation approaches based on modular, 3D printed sections for tubular heat exchangers.

Nomenclature

Symbol	Quantity	SI Unit
A	Cross-section of the tube wall	m^2
c_p	Specific heat	J/kgK
D	Tube diameter	m
f	Friction factor	-
g	Gravitational acceleration	m/s^2
H	Height of the water column	m
h	Heat transfer coefficient	W/m^2K
K	Fitting loss coefficient	-
L	Length of the heated section	m
l	Distance between heated and non-heated sections	m
Nu	Nusselt number	-
P	Pressure	Pa
Pr	Prandtl number	-
Q	Power	W
q	Heat flux	W/m^2
q_g	Generated heat	W/m^3
Q_m	Mass flow rate	kg/s
Q_v	Volumetric flow rate	m^3/s
r	Radius	m
Re	Reynolds number	-
S	Convective heat transfer surface area	m^2
T	Temperature	K

(continued on next page)

* Corresponding author.
E-mail address: luca.pagliarini@unipr.it (L. Pagliarini).

https://doi.org/10.1016/j.ijheatmasstransfer.2026.128449
Received 17 December 2025; Received in revised form 21 January 2026; Accepted 26 January 2026

(*continued*)

t	Time	s
V	Volume	m^3
v	Velocity	m/s
x	Axial coordinate	m
ΔP	Pressure difference	Pa
$NRMSD$	Normalized root mean square deviation	%
γ	Geometrical characteristics of the insert	-
δ	Uncertainty	-
ε	Emissivity	-
η	Performance index	-
θ	Circumferential coordinate	rad
λ	Thermal conductivity	W/mK
μ	Dynamic viscosity	Pa·s
ρ	Density	kg/m^3
φ	The percentage discrepancy between the provided and estimated power inputs	%
Subscripts/Superscripts		
0	Reference	
b	Bulk	
cond	Conduction	
corr	Correlation	
dist	Distributed	
el	Electrical	
exp	Experimental	
f	Fluid	
loc	Localized	
loss	Energy losses	
max	Maximum	
net	Net of losses	
s	Solid	
w	Wall	

1. Introduction

Energy efficiency in industries is nowadays crucial to meet the requirements set by net-zero emissions standards [1]. Higher efficiency is also viable to implement cost-effective measures within the manufacturing sector worldwide [2]. Among manufacturing processes, thermal treatment of products accounts for about 20 % of the total energy consumption in industrial plants [3]. Hence, deep optimization of heating and cooling systems can significantly drop the overall primary energy use. In the past decades, many scholars have proposed effective heat transfer enhancement techniques capable of beneficially affecting the fluid flow in terms of boundary layer disruption and increased turbulence. Such solutions can be categorized as active or passive heat transfer enhancement methods [4]. In particular, the former methods rely on external power in the form of magnetic/electric fields or mechanical actuators, while the latter passively operate through modified/extended surfaces or turbulators [5]. For the sake of energy efficiency, passive solutions are thus generally preferred to active ones, unless high performance control is required [6].

Among passive heat transfer enhancement technologies, recent advancements have been carried out in the definition of novel insert geometries. Wang et al. [7] studied novel V-shaped perforated rectangular winglet vortex generators for turbulent flows in cylindrical tubes by means of numerical simulations. Different geometrical characteristics, including surface area and number of winglets, were investigated. Friction factors and Nusselt numbers by varying Reynolds numbers were compared to estimate performance indexes. The maximum performance index reached a value of 1.4 for the 6 winglets having frontal area of 10 mm^2. A peculiar geometry resulting from the combination of twisted tapes and special rings was proposed by Assaf et al. [8]. Numerical results were provided for turbulent Reynolds of nanofluids at varying pitches of both the twisted tapes and the rings. The combination of two integrated passive solutions (twisted tapes and rings) and an Al_2O_3–CuO/water nanofluid guaranteed a maximum performance index of 3.29. Disc turbulators at different angular ratio and pitch were experimentally and numerically analyzed by Banihashemi et al. [9]. The inserts were centered at the tube axis by means of a metallic shaft, and they were studied in both a stationary (passive) and a rotative (active, from 300 to 600 rpm) operation. Reynolds numbers greater than 5000 were taken into account. Maximum performance index was achieved up to 1.5 for the rotational inserts. The thermofluidic performances of similar disc inserts concepts having complex, perforated/grooved geometries were numerically investigated by Mei et al. [10,11]. Additional examples of numerical explorations on particularly complex inserts in terms of heat transfer augmentation are shown in [12] and [13,14]. Butterfly inserts have been achieving increasing interest among scholars since they represent valuable and simple solutions for heat transfer enhancement via additional induced turbulence and boundary layer disruption. Pandey and Madanan [15] adopted butterfly inserts in mini-channel heat sinks to numerically define the effects of different pitch distances and pitch ratios (pitch distance divided by hydraulic diameter) in the overall thermal performance. The carried-out simulations considered the presence of a rod (diameter = 0.3 mm) holding the inserts in position, even though its implementation in real microsystems might be practically unfeasible. The values of performance indexes were here found to be greater than 1.6 in the range 200– 900 *Re*. In laminar conditions, the optimal pitch ratio was therefore found equal to 1.5. Bozzoli et al. [16] adopted infrared thermography coupled with the resolution of the Inverse Heat Conduction Problem (IHCP) to the analysis of local heat transfer in a tube equipped with butterfly inserts. The inserts were 3D printed in plastic, and they were centered via a stainless-steel rod. The Reynolds number varied within the turbulent regime range. Their results highlighted that the thermofluidic behavior of butterfly inserts may not be optimal in turbulent flows due to faster degradation of induced large-scale vortices. Similar outcomes referred to butterfly inserts within the turbulent regimes were also reported by Azari and Derakhshandeh [17]. However, no performance index was presented in [16], thus lacking a complete insert characterization at high Reynolds numbers from both the thermal and hydrodynamic standpoints. Further attempts to numerically improve the performance of a butterfly insert were carried out through morphological optimization by Pagliarini et al. [18], even though the resulting estimated performance index, once convergence was reached, still assumed values lower than unity. Novel plastic butterfly inserts, analyzed through the same technique of [16], were proposed by Cattani et al. [19]. In the turbulent regime, the butterfly geometry presenting a swirled configuration of the wings ensured an increment in the Nusselt number in between 200 % and 300 % of the one obtainable through smooth tubes. The superior thermal performance of swirled butterfly inserts was hence verified, although no additional remarks on the hydrodynamic behavior (e.g., pressure drops through the inserts) were provided.

In the light of the recent literature works, two main difficulties in terms of proper design and consequent practical implementation of butterfly inserts arise. On the one hand, the need for rigid support to hold in position the inserts arrays may increase the overall tubular heat exchangers complexity. This may also result in faulty contact between the inserts and the tube walls, hence limiting possible heat conduction from the heated/cooled wall to the fluid through the turbulators, or increased fouling related to the presence of additional surfaces in contact with the treated fluid [20]. On the other hand, to the Authors' best knowledge, no clear disclosure of the full potentialities of butterfly inserts layouts has been achieved for both laminar and turbulent regimes. In fact, whereas the application of butterfly inserts is surely beneficial in laminar flows, an optimal combination of geometrical features, such as optimal shape of the inserts and pitch distances, may ensure better performances within the most challenging flow conditions in terms of heat transfer enhancement via passive methods, i.e., turbulent flows.

The present work thus proposes to fill such literature and technological gaps by considering AM sections, in which butterfly inserts are directly integrated with the tube wall via the manufacturing process. Moreover, the investigation presents in-depth characterizations of both perforated and solid butterfly insert designs for turbulent water flows, representing an additional piece of novelty in light of the considered literature. Specifically, cylindrical tubes equipped with three different butterfly inserts are analyzed in terms of both heat transfer enhancement and pressure drops to achieve their complete thermofluidic characterization. The inserts geometries have been inspired by the promising, swirled configuration of [19]. Direct fabrication of the tubular sections is obtained by using a titanium alloy via Additive Manufacturing (AM), laser melting technique. To note, AM has become increasingly relevant for a plethora of applications during the past decades since it allows the realization, with high automatization and minimal material waste, of complex geometries, which are not usually obtainable through traditional, subtractive manufacturing procedures [21]. In the thermal engineering field, AM has been proven to be extremely useful in the fabrication of compact heat exchangers. However, most of the printed solutions often refer to entire heat exchangers, designed especially for micro or small-scale applications [22]. The present study hence represents one of the first attempts at providing a full characterization of butterfly-shaped inserts that are directly integrated into tubular geometries, i.e., AM sections that could be part of large-scale, tubular heat exchangers. AM applied to the fabrication of single parts of heat exchangers may be particularly valuable for such industrial applications in which single parts of heat transfer systems need to be replaced due to local corrosion or thermal fatigue [23]. The AM sections investigated are tested for water flows characterized by Reynolds numbers spanning from 4000 up to 14,000. Heat is supplied to the system by Joule heating in the tube's wall. Inlet and outlet water temperatures are monitored via thermocouples, while inlet an outer fluid pressures are measured via two liquid column gauges. The outer wall temperature is instead measured by means of infrared thermography over the whole tube circumference. The local and average Nusselt numbers are therefore assessed by means of the inner wall temperature at different tube sections, evaluated by applying a dedicated, analytically formulated correction to the measured outer wall temperature. A correlation for the Nusselt number, which considers both flow and geometrical conditions, is also presented. The fitting loss coefficient referred to each butterfly insert is additionally evaluated through the estimated local pressure drops. To provide a complete characterization of the analyzed solutions, performance indexes are assessed by comparing Nusselt number and friction factor increments, hence highlighting the optimal geometry to be adopted in turbulent flows from a thermofluidic standpoint. Hence, an in-depth characterization of both perforated and solid butterfly insert designs under turbulent regime is presented, emphasizing through novel pieces of results the role of insert geometries on the thermo-fluid dynamics of the AM samples.

2. AM sections: fabrication procedure and specifications

The additive manufacturing (AM) specimens investigated in the present study were fabricated by Laser Powder Bed Fusion (L-PBF), also known as Selective Laser Melting (SLM). This process builds metallic components through the successive melting and solidification of powder layers under tightly controlled conditions, ensuring high dimensional precision and material homogeneity. The samples were produced using a Renishaw© AM400 system, equipped with a continuous-wave ytterbium fiber laser operating at a wavelength of 1070 nm and a nominal maximum power of 400 W (Fig. 1). This configuration provides stable energy input and uniform melting behavior, both essential for achieving defect-free titanium alloy structures.

The build chamber was purged with high-purity argon (99.998 %) to maintain an oxygen concentration below 100 ppm throughout the process, effectively preventing oxidation and embrittlement of the titanium alloy during melting. The starting material consisted of a Ti6Al4V Grade 23 titanium alloy (ELI – Extra Low Interstitial), produced by plasma atomization. The resulting powder exhibited spherical morphology and excellent flowability, both essential for ensuring uniform layer deposition and consistent melting behavior. Particle size distribution ranged between 15 and 55 μm, with an average diameter (D50) of approximately 30 μm (Fig. 2). Maintaining an inert argon atmosphere was

Fig. 1. The 3D printer Renishaw© AM 400 used for printing the components.

critical, as titanium is highly reactive at elevated temperatures and tends to absorb oxygen and nitrogen, leading to embrittlement, contamination, and degradation of mechanical performance.

The nominal chemical composition of the Ti6Al4V Grade 23 powder is reported in Table 1. The controlled composition and the extremely low content of interstitial elements confer to the alloy an excellent balance of mechanical strength, toughness, and biocompatibility. These characteristics make Ti6Al4V ELI a reference material extensively used in aerospace, biomedical, and energy applications, where a combination of high performance and reliability is required. The chemical purity of the alloy also ensures superior corrosion resistance and long-term stability, particularly under cyclic thermal or mechanical loading conditions.

Ti6Al4V ELI was selected as the base material for the investigated components due to its favorable combination of thermal, electrical, and mechanical properties, together with its excellent processability by Laser Powder Bed Fusion (L-PBF). Although titanium alloys exhibit a lower thermal conductivity ($\sim$ 6–7 W/m·K) compared to aluminum or copper, Ti6Al4V maintains a stable heat conduction behavior even at elevated temperatures. This stability ensures uniform thermal gradients and minimizes the risk of localized overheating during both manufacturing and service. Its high melting point ($\approx 1660^{\circ}$C) further contributes to dimensional stability under cyclic thermal loading, a condition typical of heat transfer and electrically assisted flow applications. From an electrical standpoint, Ti6Al4V displays moderate resistivity ($\sim 1.7 \times 10^{-6}$ Ω·m), enabling it to act simultaneously as a structural and resistive element when subjected to Joule heating. This dual functionality allows controlled and localized heating without the need for embedded resistors or additional conductive coatings, thereby simplifying system integration and reducing interfacial losses. The relatively high resistivity, compared with pure metals such as copper, also promotes uniform heat generation within the structure, enhancing temperature control during operation. Thermally, the alloy provides low thermal expansion ($\approx 9 \times 10^{-6}$ K^{-1}) and excellent oxidation resistance, especially when processed under inert atmospheres and followed by stress-relief treatments. These properties help prevent deformation and microcrack formation during rapid thermal cycles, preserving the integrity of thin internal fins and geometrically delicate features. Moreover, the fine $\alpha + \beta$ lamellar microstructure obtained after post-processing offers an optimal balance between thermal conduction and mechanical robustness, ensuring stable performance under combined

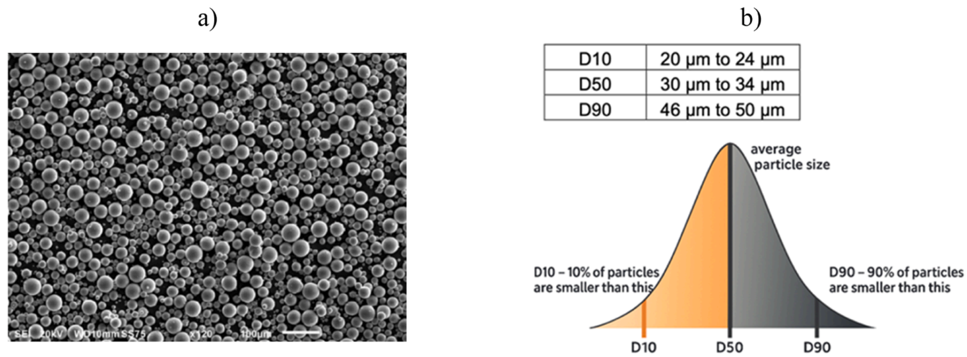

Fig. 2. Scanning electron microscope image of Ti6Al4V powder (a), and particle size distribution analyzed by laser diffraction according to ASTM B822 (b).

Table 1
Powder composition / percent by mass.

Ti	Al	V	Fe	O	Residual	C	N	H
Balance	5.5 to 6.5	3.5 to 4.5	< 0.25	< 0.13	< 0.1 each < 0.4 total	< 0.08	< 0.03	< 0.0125

thermal and mechanical stresses. Therefore, Ti6Al4V ELI represents an ideal compromise between thermal conductivity, electrical resistivity, mechanical strength, and manufacturability, making it particularly suitable for compact, thermally loaded components requiring both structural integrity and controlled heat-transfer capability. During tests, low thermal conductivity of the manufacturing alloy also allowed the establishing of higher temperature gradients, thus providing a clear experimental sign to characterize the local thermofluidic response of the fabricated samples. Hence, the choice of Ti6Al4V alloy was here further driven by experimental needs; in fact, the present investigation focused on the effects of different butterfly insert geometries on the overall thermo-fluid dynamics rather than the beneficial effects of conduction along the inserts.

The process parameters were optimized to produce components with a relative density exceeding 99.5 % and with excellent surface quality. To relieve the residual stress generated during the L-PBF process, all specimens underwent a stress-relief heat treatment at 730 °C for 2 h in a high-purity argon environment. The components were then furnace-cooled to 350 °C before the gas flow was shut off. This post-processing route effectively promotes the transformation of the metastable α' martensitic phase into a lamellar $\alpha + \beta$ microstructure, improving ductility and fatigue strength without compromising dimensional accuracy.

The geometries fabricated in this study, referred to as “butterfly inserts”, were designed as tubular AM components featuring internal swirled butterfly fins with a thickness of 2 mm. These fins serve as flow disruptors, enhancing turbulence and promoting convective heat transfer within the fluid domain. Three distinct insert configurations, namely Butterfly 1, Butterfly 2, and Butterfly 3, were produced, differing in internal topology and perforation pattern, to investigate the influence of internal geometry on both heat transfer enhancement and associated pressure drops (Fig. 3).

The specimens were built with horizontal orientation to minimize the need for support structures and to ensure optimal surface integrity of the internal channels. Metallic fins were printed at both ends of each specimen to serve as support interfaces and reference surfaces for power cable alignment and electrical connections during experimental testing. After fabrication, the parts remained attached to the build plate and underwent powder removal by compressed air followed by ultrasonic cleaning to eliminate any residual non-melted particles. Subsequently, a light bead-blasting treatment was applied to homogenize the external surface finish and improve the aesthetic uniformity of the specimens.

Before detachment from the build plate, each printed section was visually inspected to verify dimensional conformity and surface quality. Final separation was performed by wire electro-discharge machining (EDM) to preserve edge precision and prevent mechanical distortion. The different stages of the manufacturing and post-processing sequence

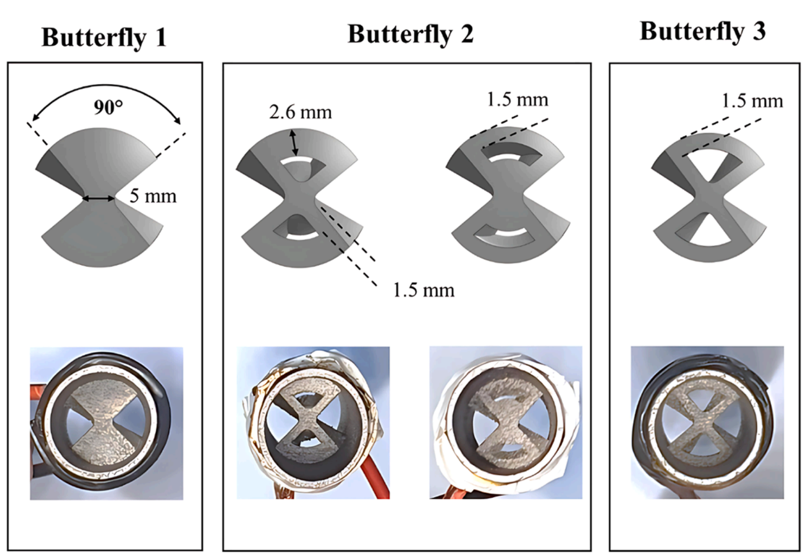

Fig. 3. Geometries of the investigated butterfly inserts.

are illustrated in Fig. 4. Fig. 4a shows the as-built components inside the L-PBF build chamber immediately after fabrication, whereas Fig. 4b presents the parts after the removal of unfused powder. Finally, Fig. 4c and d depict the specimens still anchored to the build plate, highlighting the high dimensional uniformity and surface quality obtained after powder removal and bead blasting.

The selection of Laser Powder Bed Fusion (L-PBF) technology for the fabrication of the titanium inserts was motivated by its unique capability to produce complex, internally featured geometries that are unattainable through conventional subtractive or casting methods. Additive manufacturing enables precise control of internal channels and fin geometries, which is crucial for optimizing the thermo-fluid dynamic behavior of the system. Furthermore, the design freedom inherent to L-PBF allows the integration of multiple functionalities, such as heat exchange surfaces, electrical connections, and mechanical reference features, within a single, monolithic component. This integration not only enhances functional compactness but also reduces assembly time and overall manufacturing costs. The inherent high thermal conductivity, corrosion resistance, and mechanical strength of Ti6Al4V ELI further support its application in compact heat exchangers and other thermally loaded components operating under aggressive environments. In summary, the use of the Renishaw© AM400 system enabled the production of high-density Ti6Al4V ELI samples characterized by excellent dimensional accuracy, surface finish, and microstructural reliability, thereby providing a robust foundation for subsequent experimental investigations on heat transfer and pressure drop performance in the additively manufactured butterfly inserts.

During the additive manufacturing of Ti6Al4V specimens using Laser Powder Bed Fusion (L-PBF) on the Renishaw© AM400 system, specific process parameters were carefully selected to optimize morphology, density, and mechanical performance. The base configuration employed a layer thickness of 60 µm, representing a balanced compromise between build rate and surface quality. To ensure geometric precision, gap-filling and slice-unification functions were activated with a maximum gap size of 0.1 mm, while a beam compensation of 0.12 mm was applied to correct for the actual laser beam width. Each layer's contour was defined by two border scans, spaced 0.11 mm apart and executed in an InsideOut order. The hatching pattern used a track distance of 0.10 mm with a layer-to-layer offset of –0.01 mm, and a stripe filling strategy was adopted, with a hatching angle rotated by 67° between successive layers to minimize recurring defect formation and reduce anisotropy.

The Stripe scanning strategy was implemented to optimize both part quality and process stability. In this approach, each layer surface is divided into narrow, parallel stripes that are sequentially melted by the laser. This method limits thermal deformation by allowing partial cooling between stripes, thereby reducing heat accumulation and internal stresses within the component. Alternating the orientation of the stripes between consecutive layers further enhances microstructural homogeneity by interrupting preferential solidification paths and promoting a more isotropic grain structure.

This strategy also prevents optical and thermal distortions that may arise when scanning large continuous areas. By dividing the exposure into smaller, well-controlled regions, laser power and beam quality remain more stable, resulting in consistent melting behavior and improved dimensional accuracy of the printed parts. For Ti6Al4V, the Stripe approach exerts a marked metallurgical influence, favoring the formation of a fine α' martensitic microstructure, typical of L-PBF components, with uniform phase distribution and minimal discontinuities. The refined microstructure and controlled thermal gradients significantly mitigate the risk of thermally induced cracking, a common issue in titanium alloys due to their low thermal conductivity and high residual-stress sensitivity.

Furthermore, the Stripe strategy enhances the repeatability of mechanical properties among different specimens, yielding comparable strength and hardness along the X and Y build directions. This improved isotropy indicates stable metallurgical behavior and consistent part quality. Process parameters such as laser power, exposure time, and point distance were further tuned according to specific regions of the specimens, including borders, infill, up-skin, down-skin, and support areas. For instance, the main hatching infill was processed at 350 W, while surface layers and borders were typically exposed at 200 W, with customized exposure times and point distances to control surface roughness and local density. A double-exposure (remelting) strategy was also applied to down-skin surfaces to improve interlayer cohesion and the morphology of downward-facing regions.

Overall, the combination of these process optimizations reflects best practices from recent L-PBF studies on Ti6Al4V [24], where part density, surface finish, and mechanical stability are improved through careful management of hatch spacing, energy input, scan sequence rotation, and targeted optimization of critical regions.

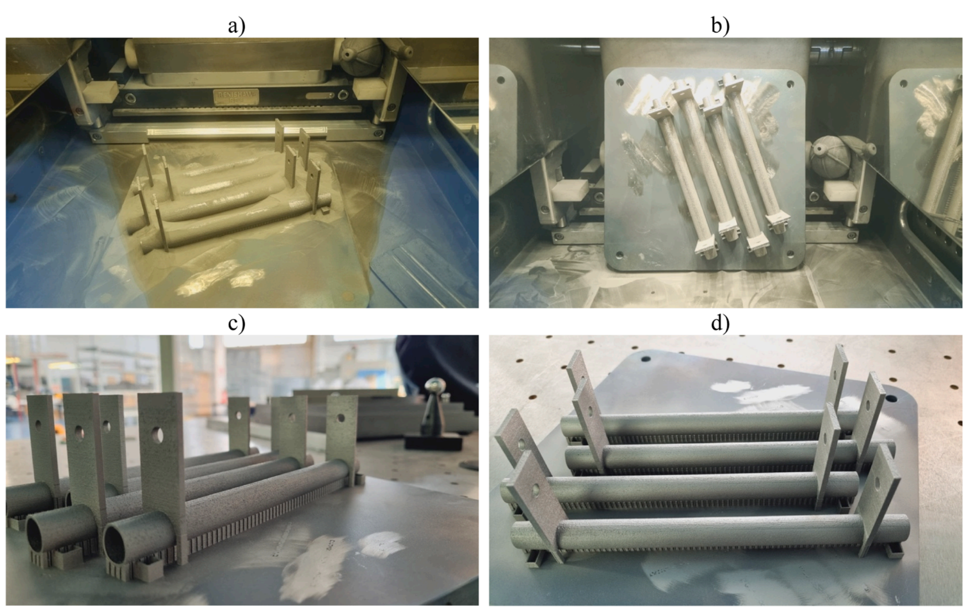

Fig. 4. Manufacturing and post-processing of Ti6Al4V components produced by Laser Powder Bed Fusion (L-PBF): (a) As-built components inside the build chamber; (b) Printed components after powder removal; (c) and (d) printed specimens anchored to the build plate.

3. Experimental set-up

The test rig is outlined by the schematic of Fig. 5a. At the inlet, a valve was used to regulate the flow rate of cold water coming from the municipal well. PVC-U pipes, having outer diameter D_{in} of 15 mm and wall thickness of 1 mm, were adopted to connect the two ends of the AM sample. Two holes were drilled in the PVC-U tubes (roughness provided by the manufacturer: $2{\cdot}10^{-4}$ m) close to the inlet and outlet of the AM section to host two liquid-column gauges (length: 2 m) for fluid pressure measurements (P_1 and P_2). The distance between the two pressure measurement points was equal to 0.94 m. Three T-type thermocouples, one placed upstream (T_1) and two downstream (T_2 and T_3) the AM sample, were inserted into the fluid stream to additionally monitor the water temperature. Specifically, T_1 was placed 6 cm away from the AM sample inlet, while T_2 and T_3 were placed 5 cm away from the AM sample outlet. Ambient temperature was monitored by an additional T-type thermocouple. All the thermocouples were connected to an Agilent© 34970A data logger. Heat was generated by Joule effect within the AM sample. Electrical power was provided by a Keysight© N8733A power supply (accuracy 0.05 % + 7.5 mV, 0.1 % + 440 mA) by means of two copper cables (cross-section = 50 mm^2), connected to the AM sample ends. Copper wires were directly wrapped around the tube over a thin layer of copper paste to improve electrical conductivity. Hose clamps further ensured effectiveness and mechanical stability of the electrical contacts. Two copper cables, connected to the power supply, were also employed to measure voltage between the two electrical connections. The distance between the two electrical connections was assessed as 0.15 m. A representative picture of the AM sample and electrical connections is shown in Fig. 6b The center of the AM section is externally coated with a high-emissivity paint ($\varepsilon \approx 0.92$) to allow IR acquisitions on the outer wall by means of a medium-wave IR camera FLIR© SC7000 (spatial resolution: 640 × 512 pixels, accuracy: ±1 K, sensitivity $\leq$ 20 mK). An additional thermocouple T_4 is attached to one side of the externally coated section. Two aluminum tape references, 0.07 m apart, were attached at the two ends of the section of interest for IR measurements. According to the reference of Fig. 5b, the butterfly insert was centered at $x = 0.026$ m.

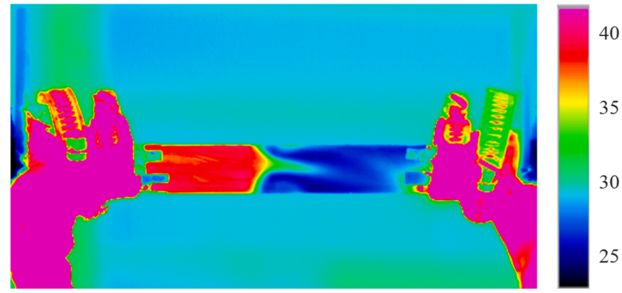

Fig. 6. Representative sample of raw IR acquisition.

During tests, water was circulated inside the pipeline. A power of Q_{el} = 277 W was supplied to the AM sample, whereas different valve openings allowed varying water flow rates. The latter were evaluated by measuring the time taken by the fluid to fill a graduated cylinder of 1 L of volume, placed at the pipeline outlet. Time measurements were repeated three times to mitigate measurement errors. In the present study, the considered Reynolds numbers ranged from about 4000 up to 14,000.

When the steady state was reached for each test condition, IR acquisitions were taken by moving the camera around the investigated section. The distance between the camera and the framed surface was kept equal to 0.56 m. Such a procedure allowed measurements of the outer wall temperature distribution in the whole AM sample. Pressure losses along the pipeline were measured, for different mass flow rates, monitoring the difference in pressure head between the two water

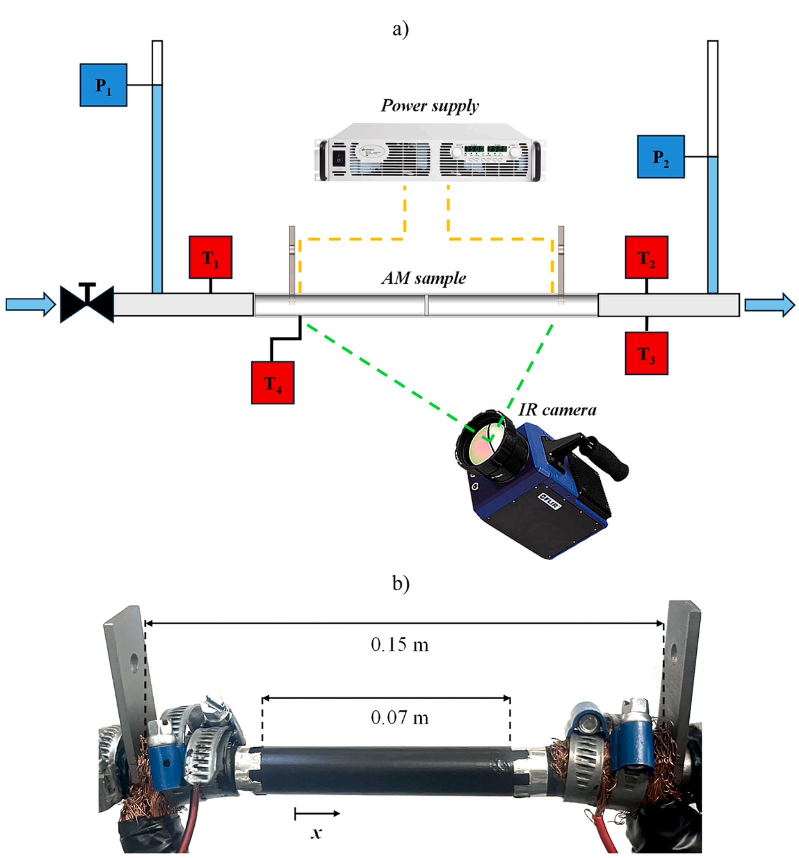

Fig. 5. Schematic of the experimental set-up (a) and picutre of the test section, with reference to the positioning of the axial coordinate origin (b).

columns through a caliper. To note, Butterfly 2 (Fig. 3) was tested at two different positions, the first with cold water flowing through the insert holes from the core of the tube to the wall (i.e., divergent holes), namely Dir 1, while, the second, from the wall to the tube core, (i.e., convergent holes), namely Dir 2.

4. Methods

In the present Section, all the procedures carried out for data acquisition and post-processing are described, along with the uncertainty analysis related to each measured or derived quantity.

4.1. Flow quantities estimation

The volumetric flow rate was first evaluated through the formulation $Q_V = \frac{V}{t}$, where V is the volume of the graduated cylinder placed at the outlet of the pipeline, and t is the measured time to fill it. The mass flow rate is therefore estimated by $Q_m = Q_v\rho$, where ρ is the density of water. To note, all the water physical properties were assessed at the average fluid temperature $T_f = \frac{T_1+T_2+T_3}{3}$ by means of the NIST mini-REFPROP software [25]. The Reynolds number related to each flow condition was estimated as $Re = \frac{vD_{in}\rho}{\mu}$, where $v = 4\frac{Q_V}{\pi D_{in}^2}$ is the fluid velocity, and μ is the dynamic viscosity of water.

The difference in pressure head between the inlet and outlet of the test section allowed the estimation of pressure drops along the tube. Such an evaluation was carried out at varying Reynolds numbers for all the butterfly inserts, as well as for the plain tube as a benchmark for the experimental procedure. Specifically, the pressure drops between the two liquid-column gauges is expressed as [26]:

$$\Delta P = \Delta H\rho g \tag{1}$$

where ΔH is the difference in height between the two water columns, and g is the gravitational acceleration. The measured pressure drops ΔP were therefore decomposed into different pressure terms to empirically estimate the fitting loss coefficients K [27] associated with the local pressure drops ΔP_{loc}, resulting from each butterfly insert geometry. In fact, the total pressure drops can be defined as:

$$\Delta P = \Delta P_{dist} + \Delta P_{loc} \tag{2}$$

where ΔP_{dist} are the distributed pressure losses. For the AM section integrated with butterfly inserts, such pressure drops are considered equal to those resulted from the plain tube configuration at same Reynolds number. Specifically, the latter are estimated by means of the Darcy-Weisbach relation [28]:

$$\Delta P = f\frac{\rho L_{tot}}{2D_{in}}v^2 \tag{3}$$

where f is the Darcy friction factor, and L_{tot} is the length of the tube, i.e., distance between pressure measurement locations P_1 and P_2 (reference of Fig. 5a). The friction factor can be recursively evaluated by means of the Colebrook equation:

$$\frac{1}{\sqrt{f}} = -2\log\left(\frac{2.51}{Re\sqrt{f}} + \frac{\epsilon/D_{in}}{3.71}\right) \tag{4}$$

where ϵ/D_{in} is the relative roughness of the tube. By estimating the ΔP_{dist} term, local pressure losses can be evaluated by means of Eq. (4). Finally, ΔP_{loc} are characterized by considering a modified Darcy-Weisbach equation, where spatial parameters are implicit, and they are included into the fitting loss coefficient K [27]:

In fact, such a value characterizes the pressure losses for each butterfly insert, and it stands as a fundamental parameter to predict pressure drops in complex systems where multiple inserts are to be employed.

4.2. Heat transfer quantities estimation

As mentioned in Section 3, IR acquisitions were taken around the AM section during steady-state conditions. In Fig. 6, a representative raw IR acquisition is shown for $Re = 4086$, Butterfly 1 (cold water flowing from left to right). To obtain meaningful temperature distributions out of the collected IR acquisitions, care should be taken in merging consecutive IR pictures along the tube circumference. The procedure leading to uniform outer wall temperature distributions from IR samples is thoroughly outlined in the work by Azam et al. [29]. It has to be stressed that the wall temperature measured at T_4 was used for *in-situ* calibration of the thermographic data. In particular, the values of parameters within the IR camera software were adjusted until a match between the thermographic temperature and the one acquired by means of the thermocouple in the same location was reached.

The outer wall temperature acquired by IR thermography is therefore adopted to estimate meaningful quantities linked to inner convection in the AM sections. Specifically, the local Nusselt number Nu_i was estimated by considering consecutive portions of the tube wall, each having length $\Delta L = 0.005$ m. At the i-th section of the AM sample, the heat flux exchanged between the wall and the fluid is defined as:

$$q = h_{in,i}\left(\overline{T}_{w,in,i} - T_{b,i}\right) \tag{6}$$

where h_{in} is the convective heat transfer coefficient at the wall-fluid interface, q is the heat flux exchanged at the wall-fluid interface, $q = \frac{Q_{net}}{\pi D_{in}L}$, being Q_{net} the thermal power net of losses to the surroundings, L is the length of the heated tube part, $T_{b,i}$ is the fluid bulk temperature of the i-th fluid element, while $\overline{T}_{w,in,i}$ is the average internal wall temperature of the i-th wall element. To note, all the quantities appearing in Eq. (6) are referred to circumferential averages in the i-th tube sections. For what concerns q, Eq. (6) is valid when two main assumptions are satisfied:

- uniformity of generated heat in the AM sample;
- axially constant heat flux exchanged between the tube wall and the fluid.

Specifically, the validity of the first assumption is discussed in Section 5.1, whereas the second assumption has been verified by Cattani et al. [30] in a previous investigation. In fact, despite local perturbations of q due to the presence of inserts, the Authors showed that the heat flux exchanged at the wall-fluid interface can be considered, on average, as constant both circumferentially and along the tube axis. On the other hand, the bulk temperature at the i-th tube section is evaluated by applying the energy balance for the corresponding i-th fluid element:

$$Q_{net,\ i} = Q_m c_p\left(T_{b,i} - T_{b,i-1}\right) \tag{7}$$

where c_p is the specific heat of water, and $Q_{net,i} = q(\pi D_{in}\Delta L)$. Starting from the inlet bulk temperature T_1 (acquired by means of the thermocouple T_1, reference of Fig. 5a), $T_{b,i}$ can be evaluated in every considered section by recursively adopting Eq. (7).

Lastly, care should be taken in evaluating values of inner tube wall temperature. Specifically, in the light of the rather low thermal conductivity of the AM sample and the expected high heat transfer coefficients, the thin-wall approximation does not hold, being the criterion based on low Biot number not satisfied [28]. Hence, the wall temperature cannot be considered as equal on both the outer and inner wall surfaces. To achieve a reasonable estimation of the inner wall temperature, the following approach, based on the analytical solution of the energy equation in the wall, is adopted.

By assuming negligible conduction along the axial and circumferential coordinates, the stationary energy equation in radial coordinates with heat generation q_g, when applied to the generic section of the tube wall, reads as:

$$0 = \lambda_s \nabla^2 T(r) + q_g \tag{8}$$

where λ_s is the thermal conductivity of the solid wall. Eq. (8) is completed by the following boundary conditions at the internal and external radii r_{in} and r_{ext}, respectively:

$$\left.\frac{\lambda dT}{dr}\right|_{r=r_{in}} = h_{in}\left(T_{w,in} - T_b\right) \tag{9}$$

$$\left.\frac{\lambda dT}{dr}\right|_{r=r_{ext}} = -h_{ext}\left(T_{w,ext} - T_{env}\right) \tag{10}$$

where T_{env} is the temperature of the external environment. After manipulation, the solution for Eq. (8) can be expressed in terms of a difference between $T(r_{ext})$ and $T(r_{in})$, i.e., temperature variation from inner and outer wall temperature, as follows:

$$\Delta T_w = T_{w,ext} - T_{w,in} = -\frac{q_g}{4\lambda_s}\left(r_{ext}^2 - r_{in}^2\right) + A\ ln\left(\frac{r_{ext}}{r_{in}}\right) \tag{11}$$

$$A = \frac{q_g r_{ext}^2}{2\lambda_s} + \frac{h_{ext} r_{ext}}{\lambda_s}\left(T_{w,ext} - T_{env}\right) \tag{12}$$

By knowing the outer wall temperature, the internal wall temperature $T_{w,in}$ is directly estimated from Eq. (11). It is worth to note that, according to the provided analytical solution under the drawn assumptions, ΔT_w does not depend on the internal heat transfer coefficient, but only on the external convective conditions. In other words, a direct knowledge of the environmental and external wall conditions allows a direct evaluation of the internal wall temperature, hence ensuring a robust assessment of the internal convective heat transfer coefficient. In fact, the average external wall temperature $\overline{T}_{w,ext,i}$ is assessed by averaging the thermographic data referred to the i-th wall section. By substituting $\overline{T}_{w,ext,i}$ into Eq. (11), the average internal wall temperature $\overline{T}_{w,in,i}$ to be inputted in Eq. (6) can be therefore assessed. The local Nusselt number is finally estimated as follows:

$$Nu_i = \frac{h_i D_{in}}{\lambda_{f_i}} \tag{13}$$

where λ_{f_i} is the thermal conductivity of water evaluated at $T_{b,i}$, while h_i comes from the resolution of Eq. (6). The average Nusselt number $\overline{Nu}$ can be further estimated by averaging the local Nusselt number along the overall test section, i.e., for the total number of considered subsections I:

$$\overline{Nu} = \frac{\sum_{i=1}^{I} Nu_i}{I} \tag{14}$$

4.3. Uncertainty analysis

The uncertainty related to each evaluated quantity was estimated by means of the propagation of errors approach by Kline and McClintock [31]. To note, in the following notation, δ represents the uncertainty associated with the considered quantity. Specifically, being a generic quantity Y derived from m quantities X affected by uncertainty, the resulting δY can be estimated as follows:

$$\delta Y = \sqrt{\sum_{j=1}^{m}\left(\delta X_j \frac{\partial Y}{\partial X_j}\right)^2} \tag{15}$$

The values of uncertainty related to the measured and derived quantities are listed in Table 2. The uncertainty related to the derived quantities are related to the maximum uncertainty assessed by means of Eq. (15).

Table 2
Uncertainty of measured quantities, and computed maximum uncertaintis of dervied quantities through propagation of error.

Measured quantities				
δt	δV	δD	δT	$\delta \Delta P$
0.1 s	10^{-5} m^3	10^{-4} m	0.1 °C	100 Pa
Derived quantities				
δRe	δQ_{el}	δh	δNu	δv
60	0.5 W	401 W/m^{2}K	8.7	0.02 m/s

5. Results

In the present section, the results referred to the effects of butterfly inserts inside the AM sections on the overall thermo-fluid dynamics are discussed. First, preliminary checks on the robustness of the experimental procedure are presented, including uniform heating, energy balance verification, and validation of the pressure drops estimations. The results referred to the induced thermal behavior of the inserts are therefore presented. Main quantities related to the inner fluid dynamics are additionally provided and discussed. Finally, the overall performance of the inserts is assessed by relating increases in local heat transfer with increases in local pressure losses.

5.1. Uniform heating in the AM section

As already mentioned, uniform heating in the AM sections was experimentally assessed. Such a test was crucial to understand and verify the thermal response of the AM samples to Joule heating. In particular, the samples were tested as empty (i.e., only filled with air) by providing a limited heat load of 2 W to prevent overheating. IR acquisitions were carried out during steady state to assess the outer wall temperature distribution. In Fig. 7, temperature profiles referred to three different circumferential coordinates $\theta = \pi/2/2$, $\theta = \pi$, and $\theta = 3/2\pi$ are shown for Butterfly 3. In every considered coordinate, the outer wall temperature exhibits a rather flat distribution, despite some variations close to the edges of the sample to be accounted for weak axial dissipation by conduction. Moreover, temperature profiles show an almost flat distribution at the insert location, probably due to additional low dissipations through the butterfly insert.

Nonetheless, the maximum deviation of temperature from circumferential coordinate to circumferential coordinate was here equal to about 0.3 °C, highlighting a good thermalization of the sample. This suggests that heat generation inside the AM sample ensures uniform heating of the tube wall, hence allowing to consider the provided electrical power Q_{el} uniformly dissipated in the conductive domain. Such uniform heating was also observed for Butterfly 1 and Butterfly 2 samples, thus confirming uniform electrical dissipation in the AM sections and, consequently, isotropic electrical conductivity of the AM titanium

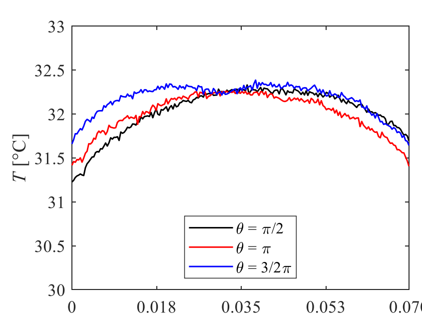

Fig. 7. Wall temperature distributions acquired by thermography at three circumferential coordinates during empty test (Butterfly 3).

alloy. Hence, the assumption drawn in Section 4.2 was considered as experimentally verified.

5.2. Energy balance verification

Another crucial preliminary check on the samples was referred to the verification of the energy balance for the water flow. First, the net heat load Q_{net} to the AM sample was estimated by considering heat dissipation to the surroundings. Such a value was therefore compared with the one assessed through the energy balance Q'_{net} to provide an evaluation of discrepancies between the two quantities, thus allowing a verification of the experimental procedure. In particular, the net power provided to the fluid is defined as:

$$Q_{net} = Q_{el} - Q_{loss,ext} - Q_{loss,cond} \tag{16}$$

where $Q_{loss,ext}$ is the power dissipated by free convection with air and radiation to the surroundings, while $Q_{loss,cond}$ is the power dissipated by axial conduction from the edges of the heated region to the lateral, non-heated parts of the AM sample. In particular, dissipations to the surroundings can be defined as:

$$Q_{loss,ext} = h_{ext}\left(\overline{T}_{w,ext} - T_{env}\right)S_{ext} \tag{17}$$

being $S_{ext} = \pi D_{ext} L$ the external heat transfer surface (L equal to 0.15 m), and h_{ext} the external heat transfer coefficient, assumed equal to 15 W/m^{2}K [32]. On the other hand, $Q_{loss,cond}$ along the axial direction of the tube is estimated by means of the Fourier's law by considering the following relationship:

$$Q_{loss,cond} = \lambda_s A\left(\overline{T}_w - T_f\right)/l \tag{18}$$

where A is the cross-section of the tube wall, $A = \frac{\pi}{4}\left(D_{ext}^2 - D_{in}^2\right)$, T_f the average water temperature, and l the distance between the heated part and the non-heated edges, estimated equal to 0.002 m. By considering a maximum wall temperature of the sample equal to 40 °C and an average fluid temperature of 18 °C, the thermal losses assume maximum value of about 2 % of the total power Q_{el} provided to the AM sample. On the other hand, by considering environmental air at 30 °C, $Q_{loss,ext}$ assumes values lower than 1 W, hence suggesting external losses as negligible with respect to the total power.

The power provided to the sample, according to the energy balance through the whole AM section, is instead expressed as:

$$Q'_{net} = Q_m c_p (T_{in} - T_{out}) \tag{19}$$

where T_{in} is the temperature acquired by means of thermocouple T_1, i.e., the inlet fluid temperature, while T_{out} is the average between the temperature values measured by thermocouples T_2 and $T_{3,}$ i.e., the outlet fluid temperature.

The percentage discrepancy between the provided and estimated power inputs was finally quantified as:

$$\varphi = |Q_{net} - Q'_{net}| \cdot 100 \,/\, Q_{net} \tag{20}$$

φ was evaluated for all the test conditions, i.e., every Re and AM section. Specifically, the maximum discrepancies were found at the highest considered Re, with values of about 14 % of the Q_{net}. Such differences are reasonably accounted for uncertainties in the Q'_{net} estimation, mainly linked to the relative uncertainties associated to the $T_{in} - T_{out}$ temperature difference. Nonetheless, given the good agreement between provided and estimated thermal powers, it can be concluded that the energy balance is satisfied for the provided experimental set-up, hence underlining the robustness of the experimental approach.

5.3. Validation of the pressure drops measurements

The measurement procedure for pressure losses was validated by considering an AM plain tube for benchmarking, i.e., without any insert geometry. Specifically, the AM sample was loaded on the experimental set-up, and the heights of water columns were measured at the two liquid column gauges. Pressure drops were therefore estimated by means of Eq. (1), and they were compared with the ones evaluated through the Darcy-Weisbach relation of Eq. (3), coupled with the Colebrook equation of Eq. (4). To note, the average relative wall roughness between that of the AM plain tube and the PVC-U tubes, weighted for the length of each tube between the two pressure measurement points, was considered for computations. The comparison between experimental and expected results is shown in Fig. 8, together with the experimental error bars (Table 2).

Despite some discrepancies between experimental and expected data, the measured samples well agree with the values predicted by the correlation. To note, such minor discrepancies almost completely lay within the uncertainty range for pressure drop measurements. Any additional deviation from the expected data could be due to either slight differences in wall roughness with respect to the value provided by the manufacturer or minor geometrical defects. Overall, the pressure drop measurement approach was considered as validated for further fluid-dynamics investigations on the butterfly inserts.

5.4. Validation of the Nusselt number estimation procedure

The approach for the Nusselt number estimation presented in Section 4.2 was preliminary validated by adopting the AM plain tube, for Reynolds number equal to 3785. The heating power was here equal to that applied to the insert-equipped samples, such as $Q_{el} = 277$ W. Specifically, the experimental local Nusselt number was compared with the one coming from the Gnielinski correlation, complemented by the Al-Arabi correction [33]. The comparison is shown in Fig. 9; experimental uncertainty for the Nusselt number are additionally included, according to the value presented in Table 2. A good agreement between experimental and expected quantities is noticeable. To note, a slight discrepancy is present at the edges of the sample probably due to heat flux redistribution by axial conduction, in accordance with what reported by previous studies [34]. Nonetheless, all the experimental data fall within a ± 25 % range for the provided correlation, confirming the goodness of the adopted experimental approach.

5.5. Thermal behavior of AM samples

In the present Section, a description of the local thermal behavior induced by the butterfly inserts in the AM samples is presented by means of both qualitative discussions on outer wall temperature distributions and quantifications of local and average Nusselt numbers for all the

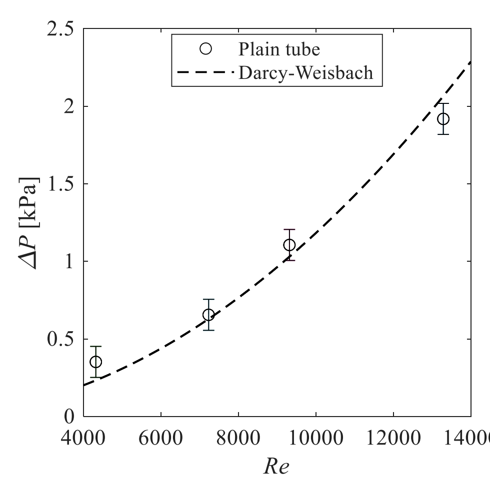

Fig. 8. Comparison between experimental and expected pressure drops.

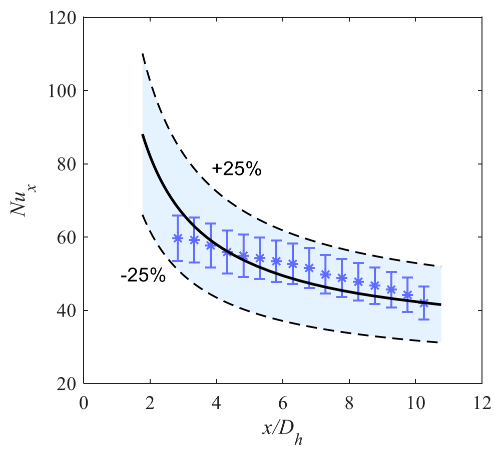

Fig. 9. Comparison between experimental local Nusselt number (blue markers) and the Gnielinski correlation with Al-Arabi correction [33] (black solid line).

geometrical configurations considered.

In Fig. 10a, a representative outer wall temperature distribution, obtained from the merging of IR maps around the tube, is shown for Butterfly 1 at Re = 4086. To note, cold fluid flows from left to right, according to the adopted geometrical reference adopted during IR acquisitions.

To provide a reference for the insert location in each reported temperature distribution, the representative picture of Fig. 10b is additionally displayed. Specifically, according to the adopted geometrical reference, inserts were circumferentially centered at angles of $3/4\pi$ and $7/4\pi$, while they were axially centered at $x = 0.026$ m (yellow boxes in Fig. 10b).

As noticeable from Fig. 10a, the wall temperature is high along the whole tube circumference upstream the insert ($x < 0.018$ m). Around the insert location, the wall undergoes a sharp cooling, probably due to induced fluid recirculation and enhanced convective heat transfer. Cooler wall areas are mainly present around the insert, while farther areas exhibit higher temperature trails that proceed up to about $x = 0.053$ m. This suggests that, in terms of local heat transfer improvement, boundary layer disruption mainly occurs closer to the insert walls, whilst farther parts of the wall are less interested by enhanced inner convective heat transfer. It has to be underlined that the hot trails at the sides of the insert are slightly inclined with respect to the tube axis. Such evidence agrees with the temperature distribution reported by Cattani et al. [19] for a similar configuration. In fact, the swirled insert geometry is here able to promote secondary flows in the axial water stream. To note, higher temperature spots at about $\theta = 3/4\pi$ and $\theta = 7/4\pi$, i.e., center of inserts wings, are present in the distributions. This may be accounted for the fact that the contact surface between the insert and the tube wall is only subjected to conductive rather than convective heat transfer, hence reducing heat dissipation at the wall. Downstream the insert ($x > 0.035$ m), the wall remains generally colder than the upstream tube sections, suggesting a persistent and beneficial effect of the insert geometry along the axial coordinate. Nonetheless, at the right edge of the observation window ($x > 0.06$ m), a weak temperature increase can be perceived in the wall, probably due to progressive degradation of heat transfer enhancement effects far from the insert location.

To better outline the effect of different insert geometries, the outer wall temperature distributions for Butterfly 2 (Dir 2) and Butterfly 3 (Re = 4086) are shown in Fig. 11a and 11b, respectively. Here, Butterfly 2 exhibits a slightly longer warm area before the insert location than Butterfly 1 (Fig. 11a). This is possibly linked to the fact that the presence of small holes in Butterfly 2 (Fig. 3) increases the cross-sectional area to be used by the fluid to flow through the insert location, hence resulting in lower bulk accelerations and consequently lower convective heat transfer. Moreover, the warm trails at the sides of the insert are wider, suggesting that Butterfly 2 enhances heat transfer at the wall-fluid interface in a narrower portion of the tube circumference. However, warmer spots at the insert wings are less evident than Butterfly 1, mainly due to higher cooling capability of fluid flowing through the holes in the insert. Lastly, Butterfly 2 denotes warmer areas at the edge of the observation window, suggesting that heat transfer enhancement decays faster than in Butterfly 1 due to lower perturbation of the fluid stream. For what concerns Butterfly 3 (Fig. 11b), the warm area upstream the insert is significantly longer, and longer hot trails at the sides of the insert are perceived. In fact, the larger holes in the insert are supposed to

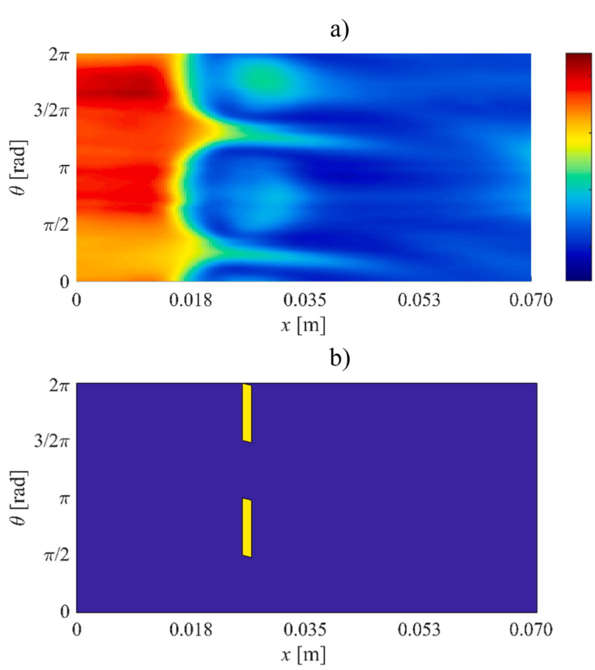

Fig. 10. Outer wall temperature distribution for Butterfly 1, Re = 4086 (a). Reference for the insert wings location in the outer wall temperature distribution (yellow boxes, b).

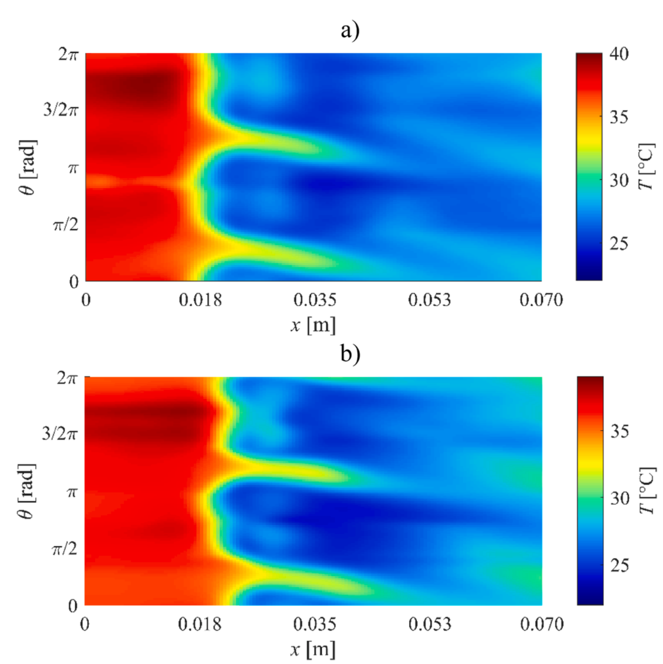

Fig. 11. Outer wall temperature distributions at Re = 4086 for Butterfly 2 (a; Dir 2) and Butterfly 3 (b).

highly hamper any fluid perturbation or acceleration, leading to lower cooling effect on the wall. The weaker effect of Butterfly 3 in terms of wall cooling is further highlighted by the longer warm areas downstream the insert, that suggest, at least qualitatively, weaker heat transfer augmentation in the test section.

The local effects on the wall temperature produced by the inserts are additionally discussed. In Fig. 12, the outer wall temperature profiles along the tube axis for fixed circumferential coordinate $\theta = 7/4\pi$ are presented.

Butterfly 1 denotes here a greater wall overheating at the insert location ($x = 0.026$ m), while the wall temperature decreases downstream. For Butterfly 2 and Butterfly 3, the overheating at the insert location progressively vanishes due to lower fluid perturbations, coupled with better cooling of the butterfly wings thanks to the presence of holes in the inserts geometry. In addition, downstream the insert, first temperature decreases are followed by progressive increases in wall temperature, confirming lower and lower heat transfer capabilities of the inserts geometry. It is also interesting to note that, from Butterfly 1 to Butterfly 3, the overheated sections not only decrease in amplitude, but also in width. This could be accounted for fluid stagnation areas, especially downstream Butterfly 1, which hampers wall cooling due to possible drops in the local convective heat transfer coefficient.

Wall temperature distributions were also investigated at varying Reynolds numbers to assess differences in thermal response resulting from higher turbulence of the fluid flow. In Fig. 13a, the wall temperature profiles along the circumferential coordinate are shown for Butterfly 1, $Re = 6827$ and $Re = 12{,}818$, at the fixed axial location $x = 0.026$ m (i.e., insert location). Here, four main temperature peaks can be noted for $Re = 6827$, two centered at the contact surface between the wings and the wall ($\theta = 3/4\pi$ and $\theta = 7/4\pi$), and two referred to the lateral hot trail at the two sides of the insert ($\theta \approx \pi/4$ and $\theta \approx 5/4\pi$). When Re increases up to 12,818, the peaks related to the hot lateral trails tend to decrease in amplitude due to the higher fluid velocity and consequently greater convective heat transfer. However, the wall temperature seems to remain unchanged at the wings locations, denoting similar temperature peaks at higher Reynolds number. This suggests that, despite an overall increase in inner convection, heat cannot be effectively dissipated at the tips of the insert wings, probably because of the low thermal conductivity characterizing the adopted titanium alloy, coupled with strong fluid stagnation downstream. In Fig. 13b, temperature profiles referred to the same Reynolds numbers and circumferential coordinate are shown for Butterfly 3. Wall temperature peaks are perceivable in the only lateral hot trails of the insert ($\theta \approx \pi/4$ and $\theta \approx 5/4\pi$) for $Re = 6827$, while no predominant peaks are noticeable at the wings locations. As long as the Reynolds number increases, the wall temperature profile decreases in amplitude along the whole circumference of the tube. This confirms the better heat transfer in both the lateral hot trail areas and the wings locations with respect to Butterfly 1, due to the presence of holes in the insert promoting cooling of the butterfly insert tips by convection.

To provide a quantitative description of the thermal response of the system induced by the presence of inserts, the local Nusselt number was estimated for every AM sample, according to the procedure of Section 4.2. In Fig. 14, Nu is shown as a function of the axial coordinate and the Reynolds number for Butterfly 1 (Fig. 14a), Butterfly 2 (Fig. 14b, Dir 2), and Butterfly 3 (Fig. 14c). For what concerns Butterfly 1, the Nusselt number starts increasing, for all the considered Re, before the insert, while it undergoes a change in slope in correspondence of the insert location $x = 0.026$ m, as well as in the subsequent fluid stagnation area discussed in Fig. 12. It has to be stressed that, when the local Nusselt number is estimated at the insert location, the corresponding heat transfer coefficient is not here to be intended as a coefficient of convection only, but as a global heat transfer coefficient that includes both convective and conductive heat transfer in the tube wall. Nu therefore keeps increasing, it reaches a maximum at $x = 0.045$ m, and it decreases far from the insert.

Such a trend reflects that the insert allows heat transfer augmentation in the AM sample. This is especially true downstream, where fluid recirculation and boundary layer disruption effects result in a significant increase in the local Nusselt number. Moreover, the increase of Nu with Re is in accordance with the well-known Reynolds analogy [35], thus confirming the validity of the results. The decrease in Nusselt number downstream the insert is also higher for higher Reynolds number, probably due to the fact that greater Reynolds numbers promote faster recovery of the boundary layer after induced disruption by the insert [36]. When Butterfly 2 is instead considered (Fig. 14b, Dir 1), the local Nusselt number exhibits a steeper increase around the insert, suggesting that such configuration is capable of significantly reducing fluid stagnation. In addition, Nu reaches lower peaks with respect to Butterfly 1, confirming lower induced heat transfer. Nonetheless, for all the considered Re, the decay in Nu with the axial coordinate is less pronounced, suggesting higher stabilization of the heat transfer enhancement effect of the insert than Butterfly 1. Lastly, Butterfly 3 (Fig. 14c) denotes a low increase in local Nusselt number for all the Reynolds numbers, confirming the poor augmentation in heat transfer capability of the fully drilled insert. Increase in Nu around the insert location is however highly continuous, thus underlining absence of any fluid recirculation areas downstream and good heat removal from the insert wings.

The local thermal behaviour of the investigated samples is globally outlined in Table 3, where the maximum values of local Nusselt number reached within the observation window are reported along with the axial coordinates corresponding to such peaks, x_{max}, for every insert geometry and considered Reynolds numbers. It has to be underlined that x_{max} varies with the insert type. In particular, holes in the insert geometry tend to move the location of maximum Nu upstream due to reduced fluid stagnation. For what concerns the two configurations of Butterfly 2, it is noticeable that Dir 1, i.e., divergent holes, is beneficial for anticipating the location at which Nu_{max} occurs with respect to Dir 2, i.e., convergent holes. This could be due to the combination of two main factors related to the induced flow motion for Dir 1, characterized by cold fluid in the core of the tube directed towards the wall. First, fluid stagnation downstream the insert might be reduced, to some extent, by means of the adopted configuration. Second, the outer wall might be

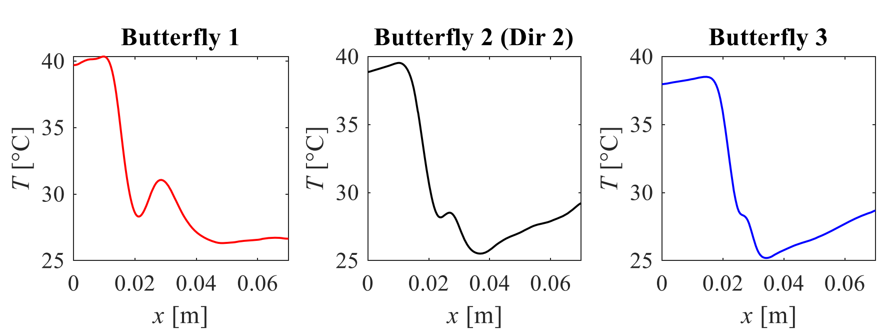

Fig. 12. Wall temperature profiles along the tube axis at fixed circumferential coordinate $\theta = 7/4\pi$ (i.e., location of inserts wings).

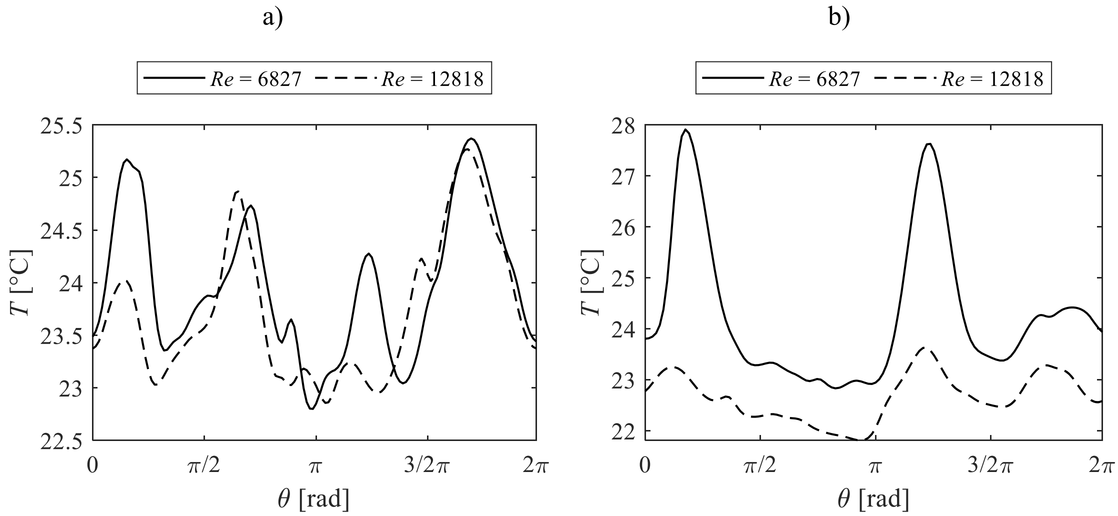

Fig. 13. Outer wall temperature profile along the insert circumeference for fixed axial location $x = 0.06$ m (center of the butterfly insert). Butterfly 1 (a); Butterfly 3 (b).

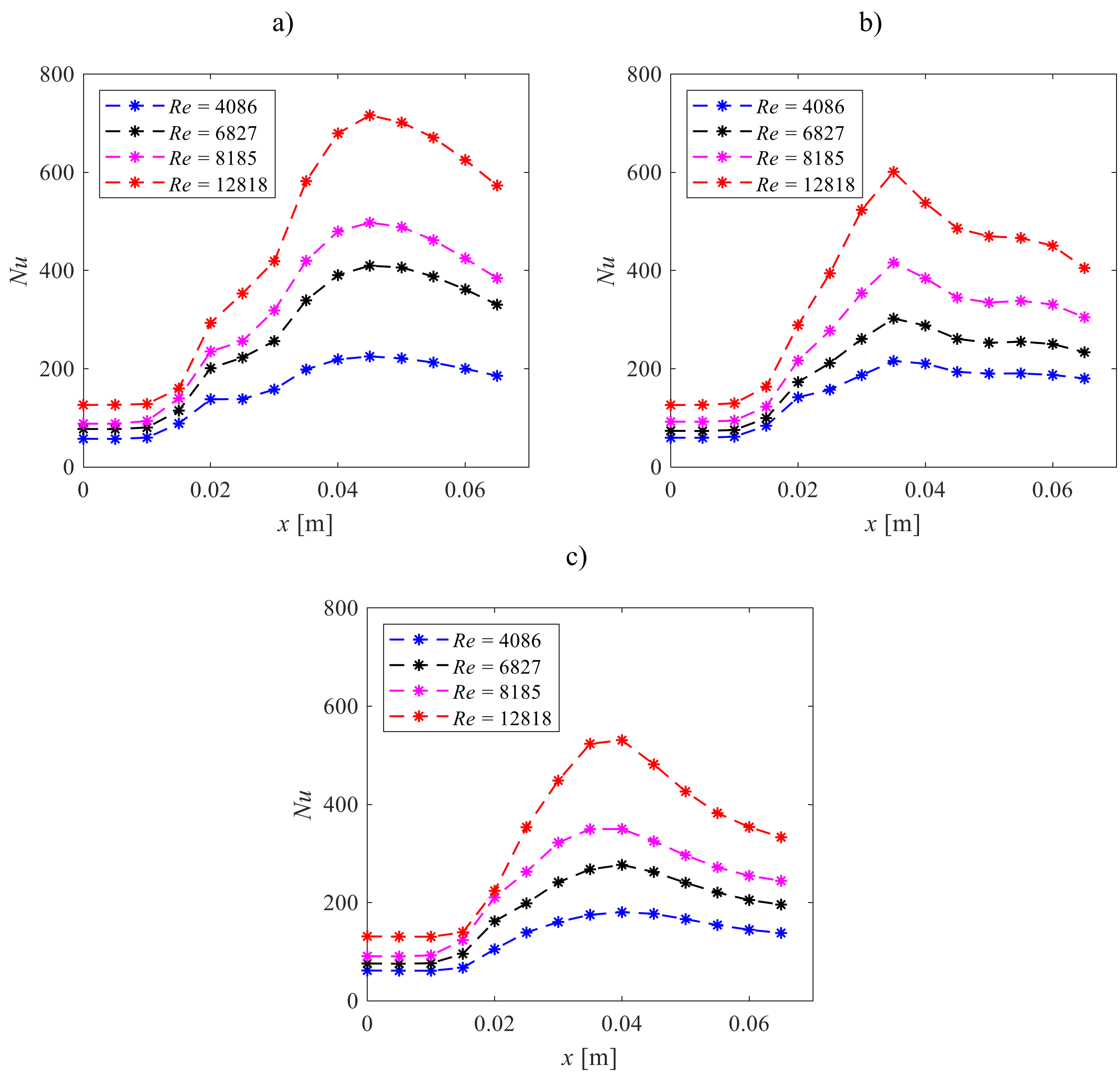

Fig. 14. Local Nusselt number as a function of the axial coordinate and the Reynolds number for butterfly 1 (a), Butterfly 2 (Dir 2, b) and Butterfly 3 (c).

Table 3
Maximum peaks of local Nusselt number, and corresponding axial coordinates.

		Re			
		4086	*6827*	*8185*	*12,818*
Butterfly 1	x_{max} [m]	0.045	0.045	0.045	0.045
	Nu_{max}	225	410	498	716
Butterfly 2 (Dir 1)	x_{max} [m]	0.03	0.03	0.03	0.03
	Nu_{max}	193	266	412	610
Butterfly 2 (Dir 2)	x_{max} [m]	0.035	0.035	0.035	0.035
	Nu_{max}	216	302	416	601
Butterfly 3	x_{max} [m]	0.04	0.04	0.04	0.04
	Nu_{max}	181	277	350	530

subjected to better cooling just after the insert, hence allowing an anticipated increment of local Nusselt number closer to the insert. Nonetheless, Dir 1 and Dir 2 exhibit comparable values of Nu_{max} for all Reynolds numbers, suggesting similar overall heat transfer augmentation. For Butterfly 3, a slightly higher x_{max} with respect to Butterfly 2 (especially for Dir 1) may be linked instead to the fact that, despite the holes prevent any recirculation downstream the insert, they do not promote any cold/warm fluid conveying. Hence, warmer fluid that flows close to the heated wall upstream tends to similarly lap the wall downstream, resulting in a lower heat transfer enhancement just after the insert.

For all configurations, it can be concluded that the local thermo-fluidic behavior induced by the inserts may be due to momentum and energy transfer promoted by the energy cascade from larger to smaller eddies, in accordance with previous findings [37]. For what concerns the two considered configurations of Butterfly 2, Dir 1 may be responsible for earlier flow reattachment with respect to Dir 2, hence promoting boundary layer disruption close to the insert location. Core-to-wall momentum transport may be therefore achieved through eddies breakdown, effectively perturbing the boundary layer at the reattachment location. Nonetheless, complete clarification on the underlining mechanisms could be only achieved through dedicated direct fluid visualizations or numerical investigations.

Finally, the values of average Nusselt number $\overline{Nu}$ are shown as a function of the Reynolds number in Fig. 15. The Nusselt number for the fully developed flow in the plain tube, computed through the Dittus-Boelter correlation (fluid being heated) [28], is also included in the graph for comparison.

Here, Butterfly 1 exhibits the highest heat transfer enhancement for all Reynolds numbers. Such a remark is reasonable, since Butterfly 1 is supposed to promote the strongest fluid disturbance. On the other hand, Butterfly 3 allows lowest heat transfer augmentation with respect to the plain tube. The maximum perceived increment of $\overline{Nu}$ was quantified, for

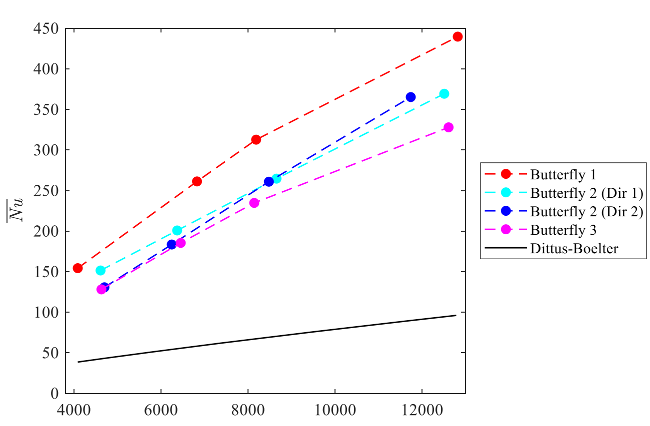

Fig. 15. Average Nusselt number as a function of the Reynolds number for all the geometrical configurations.

Butterfly 1, as about 400 % of the $\overline{Nu}$ referred to the benchmark case. Such an enhancement was in line with the one reported in [30] for a similar swirled insert and comparable Reynolds numbers. However, it should be noted that the lower augmentation reported in the previous work was probably due to longer considered areas of interest, which could have resulted in lower estimated average Nusselt numbers due to a more complete re-development of the thermal boundary layer downstream the insert. For what concerns Butterfly 2, both Dir 1 and Dir 2 configurations highlight similar values of $\overline{Nu}$, especially at high Reynolds numbers. In fact, for turbulent flows, the effect of fluid vehiculation ensured by the holes geometry is supposed not to be as predominant as for the case, for instance, of laminar flows, where fluid follows instead smooth paths in layers. Nonetheless, Dir 1 seems to present higher values of $\overline{Nu}$ than Dir 2, especially at Re lower than 7000. This could be due to the fact that, in the case of less fluid turbulence, divergent holes may allow for better wall cooling, i.e., ensuring moderate enhancement in heat transfer at the wall.

As further attempt of data reduction, the values of $\overline{Nu}$ of Figure were fitted via the *nlinfit* function within the Matlab© (v. 2022b) environment. Specifically, a correlation of the following form was adopted:

$$\overline{Nu}/Pr^{0.4} = c\gamma^{e_1} Re^{e_2} \tag{21}$$

where γ is the ratio between frontal surface of the generic butterfly insert and the total cross-sectional area of the tube, and c, e_1 and e_2 are the correlation coefficients. γ assumed values equal to 0.65, 0.55, 0.53, and 0.47 for Butterfly 1, Butterfly 2 (Dir 1), Butterfly 2 (Dir 2), and Butterfly 3, respectively. The coefficients obtained from non-linear fitting of the experimental data are listed in Table 4.

It has to be stressed that the found exponent for the Reynolds number, e_2, assumes here a value comparable with correlations provided for the case of passive heat transfer enhancement systems adopted in turbulent regimes [38,39].

The Normalized Root Mean Square Deviation (NRMSD) was estimated, for the correlation provided, as a parameter of goodness of fit:

$$NRMSD = \left[\frac{\sqrt{\frac{1}{P}\sum_{p=1}^{P}\left(Y_{exp,p} - Y_{corr,p}\right)^2}}{\overline{Y}_{exp}} \right] x\,100 \tag{22}$$

where $Y_{exp,p}$ and $Y_{corr,p}$ represent the p-th experimental and predicted quantities, respectively, while $\overline{Y}_{exp}$ is the average of all the experimental quantities. For the present case, $NRMSD$ assumed a value of about 11 %, suggesting limited deviation between experimental and predicted values of $\overline{Nu}/Pr^{0.4}$.

In Fig. 16, the comparison between predicted and experimental data is graphically shown. The *exp* and *corr* subscripts represents the experimental and predicted values, respectively. Here, it is clear that the predicted values of $\overline{Nu}/Pr^{0.4}$ well agree with the ones estimated during experimental observations, for all the considered flow regimes and geometrical configurations. All the deviations between predicted and evaluated results fell in between a confidence range of ± 15 %, hence confirming the high correlation capability of the model. Nonetheless, it should be noted that the provided correlation is expected to well predict the thermal behavior of butterfly-shaped inserts only within the

Table 4
Coefficients for correlation of Eq. (21).

Coefficient	Value
c	0.06
e_1	0.86
e_2	0.92

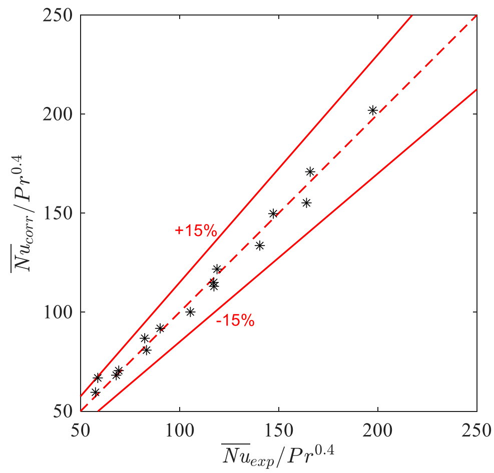

Fig. 16. Comparison between predicted and experimental $\overline{Nu}$ $/Pr^{0.4}$.

considered applicability ranges, such as $4000 < Re < 14{,}000$ and $0.47 < \gamma < 0.65$. Due to the limited number of tested geometries, the correlation provided is intended to be regarded as preliminary, and it should be thus complemented/confirmed by future investigations dealing with different obstructed flow areas and Reynolds numbers. Further analyses could also shed light on the full validity of the γ parameter in the framework of the provided correlation. In fact, while previous experimentations suggest that the induced thermal behavior could be predicted by mainly considering the flow obstruction area [36], the peculiar morphology of the adopted butterfly insert, e.g., different wings/holes shape, may also play a critical role.

A final remark was referred to the adoption of Butterfly 2 as a passive heat transfer augmentation solution. As noticeable from Fig. 15, the high similarity between the Nusselt number trends of Dir 1 and Dir 2 led to the conclusion that the flow direction impacting on the Butterfly 2 surface did not affect, on average, the overall heat transfer, at least for the turbulent flows considered. Hence, only Butterfly 2, Dir 1, will be taken into account in the following Sections, being such a case representative of both flow directions.

5.6. Fluid dynamics of AM samples

The AM samples were also analyzed in terms of fluid dynamics effects to relate heat transfer augmentation with pressure drops induced by the inserts. In Fig. 17, the experimental pressure drops are shown for the three considered butterfly inserts, as well as for the plain tube geometry for comparison.

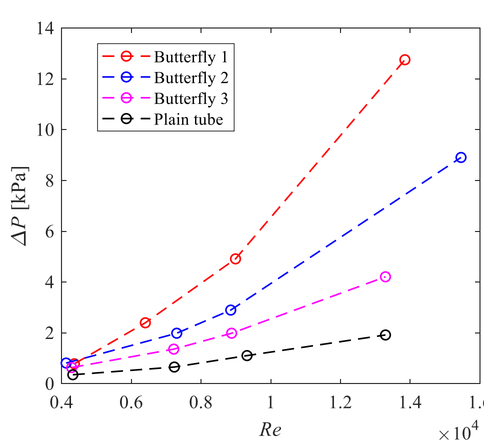

Fig. 17. Pressure drops along the test section for all the AM samples considered.

Here, it can be noted that all butterfly inserts present higher ΔP than the plain tube, and the pressure drops increase from Butterfly 3 to Butterfly 1. By considering the results of Fig. 15, this confirms what is expected from the analogy between heat transfer and pressure drops, i.e., heat transfer enhancements are always coupled with higher pressure drops in the fluid flow [35]. Such hydrodynamic behavior is, in fact, due to lower cross-sectional area available for the fluid flow through Butterfly 1 with respect to Butterfly 2 and Butterfly 3.

Finally, the K coefficients were estimated by means of Eq. (5). Specifically, the experimental local pressure losses were computed by performing the difference between the experimental pressure drops of Fig. 15 and the ones estimated through the Weisbach-Darcy relation, coupled with the Colebrook equation, at same Reynolds numbers. For each j-th butterfly insert, K_j was computed as the average of all the K coefficients at varying Reynolds numbers, while its associated estimation error was assessed as the standard deviation of all K at varying Reynolds numbers. To note, the distributed pressure losses were considered as equal in both the AM plain tube and in the samples equipped with butterfly-shaped inserts. Such an assumption was considered as reasonable, since the pipeline between the two pressure gauges (connection tubing, valves, etc.) did not undergo any substantial modification between the tests. Moreover, all the AM samples shared same roughness, according to the manufacturer.

The evaluated K are reported in Table 5, together with their percentage estimation errors.

As noticeable, K increases from Butterfly 3 to Butterfly 1, in agreement with the pressure losses trends of Fig. 17. The maximum estimation error for K was assessed equal to 13.2 %, by considering the uncertainties of both pressure drops and fluid velocity values of Section 4.3.

Such a coefficient is crucial for predicting pressure losses in more complex systems, hence instrumented with more than one insert. In particular, by knowing the flow characteristics of the investigated flow, the local pressure losses could be estimated, for combinations of in-series inserts, by adopting Eq. (5).

5.7. Overall performance of AM samples

The overall performance of the given inserts was established by means of a comprehensive method based on performance evaluation plots, originally conceptualized by Fan et al. [40], to address energy-saving characteristics of the proposed heat transfer augmentation solutions. It has to be underlined that such technique, based on the first law of thermodynamics, was chosen among other criteria due to greater generality of provided outcomes. Specifically, the performance index η_i referred to the i-th constraint, either for identical pumping power ($Q_p/Q_{p,0} = 1$), identical pressure drops ($\Delta P/\Delta P_0 = 1$), or identical flow rate ($Q_m/Q_{m,0} = 1$), reads as:

$$\eta_i = \left(\frac{\overline{Nu}}{Nu_0}\right) \Big/ \left(\frac{f}{f_0}\right)^{k_i} \tag{23}$$

where the subscript 0 refers to the benchmark geometry, i.e., the plain tube. Through a logarithmic manipulation, heat transfer enhancement can be related to friction factor increases by means of the relationship:

$$\ln\left(\frac{\overline{Nu}}{Nu_0}\right) = b_i + k_i \ln\left(\frac{f}{f_0}\right) \tag{24}$$

Table 5
K and percentage error for each butterfly insert.

	K	*Estimation error (%)*
Butterfly 1	15.6	12.1
Butterfly 2	9.6	10.5
Butterfly 3	4.9	13.2

where b_i indicates, for each adopted constraint, whether the heat exchanged in the proposed configuration is higher ($b_i > 0$) or lower ($b_i < 0$) than that of the reference case. Such a coefficient mathematically represents the quantity ln (η_i). On the other hand, the coefficient k_i assumes the following values for internal, turbulent flows, depending on the provided constraints [40]:

- $k = 1/3$ for identical pumping power.
- $k = 1/2$ for identical pressure drops.
- $k = 1$ for identical flow rate.

It can also be stressed that higher k results in higher heat transfer augmentation with respect to friction factor. Hence, heat transfer enhancement, coupled with limited friction factor increases, is an easier condition to reach under identical pumping power rather than identical pressure drops or identical flow rate. In fact, the latter represents the hardest condition to achieve for heat transfer augmentation purposes.

The baselines provided by Eq. (24) for the three different constraints, defined by null b_i coefficients (hence, $\eta_i = 1$), are shown on the performance evaluation plot of Fig. 18 together with the working points referred to the three butterfly inserts. To note, for each butterfly insert, the pressure drops of Fig. 17 were interpolated by means of a power law of the form $\Delta P = aRe^2$. Hence, the pressure losses could be directly quantified at the query points. This was particularly useful to compute the friction factors in Eq. (3) for those cases in which $\overline{Nu}$ and ΔP were evaluated at slightly different Reynolds numbers. All the interpolations were characterized by a coefficient of correlation R^2 greater than 0.99.

The baselines divide the quadrant of Fig. 18 into four meaningful regions, which can be interpreted as follows:

- Region 1 is the most unfavorable in terms of energy saving, since heat transfer enhancement is less than friction factor increases.
- Region 2 is characterized by heat transfer enhancement under identical pumping power.
- Region 3 and Region 4 are defined by augmented thermal performance under equal pressure drops and equal flow rate, respectively.

According to the previously mentioned characteristics of Eq. (24), Region 4 thus represents the most favorable section in terms of energy saving. In the chart, the working points referred to Butterfly 1 fall within Region 3, hence suggesting augmented performance under identical pressure drops. On the other hand, working points referred to both Butterfly 2 and Butterfly 3 belong to Region 4, verifying their superior performance in the most unfavorable case of identical flow rate. This remark is probably linked to the fact that holes in the butterfly inserts promote enhanced heat transfer performance with highly mitigated frictional losses, in accordance with previous studies [41,42]. Hence, Butterfly 2 and Butterfly 3 were found to have augmented performance with respect to the full insert of Butterfly 1.

To finally identify the optimal butterfly-shaped insert, the performance index referred to the identical flow rate constraint ($k = 1$) was evaluated and plotted in Fig. 19 for the only Butterfly 2 and Butterfly 3. Specifically, the performance index is rather stable for all the investigated Re and geometries. In fact, due to the intrinsic chaoticity of turbulent flows, increased turbulence is not supposed to significantly enhance heat transfer with respect to pressure drops, in accordance with previous findings [43–45]. For Butterfly 2 and Butterfly 3, η assumes values, on average, equal to 1.4 and 1.9, respectively. The found values of performance index are in line with previous investigations on heat transfer augmentation systems [46,47]. Such a remark suggests that Butterfly 3 mitigates pressure losses inside the pipe, despite the lower heat transfer enhancement produced. Hence, Butterfly 3 can be considered as the best option from an applicative standpoint, especially when an optimal trade-off between heat transfer augmentation and pressure drops is required. It has to be underlined that, despite Butterfly 3 represents the most convenient insert from the energy saving point of view, it highlights the lowest heat transfer augmentation, suggesting that its application may not be optimal for all possible applications. For instance, such industrial fields requiring highest heat transfer augmentation regardless of high increments in pressure drops would benefit more from the adoption of heat exchangers equipped with Butterfly 1 inserts, as for the case of nuclear and pharmaceutical/chemical industries, where safety and process control are prioritized with respect to pumping costs [48].

To complete the analysis on heat transfer augmentation provided by the present solutions, the main evaluated quantities are compared with those typically obtained through AM. In Table 6, the average Nusselt number, the Nusselt increment with respect to reference case, the performance index, and the k_i coefficient are reported, where possible, for recent works taking advantage of AM technology to increase heat transfer in heat exchangers.

As noticeable, AM-based methodologies represent viable solutions for heat transfer enhancement in heat exchangers. From the collected references, the present butterfly-shaped inserts exhibit heat transfer augmentation in line with typical techniques based on modified/minimal surfaces and fins, further confirming the technological advantage of the proposed butterfly-shaped inserts.

6. Conclusions

Different additive manufactured samples presenting butterfly inserts were experimentally studied to understand the effects of their integration into tubular geometries on the induced thermo-fluid dynamics. The samples were manufactured by laser melting technique by using a titanium alloy. The low thermal conductivity of the manufacturing material was specifically chosen to enhance the establishing of temperature

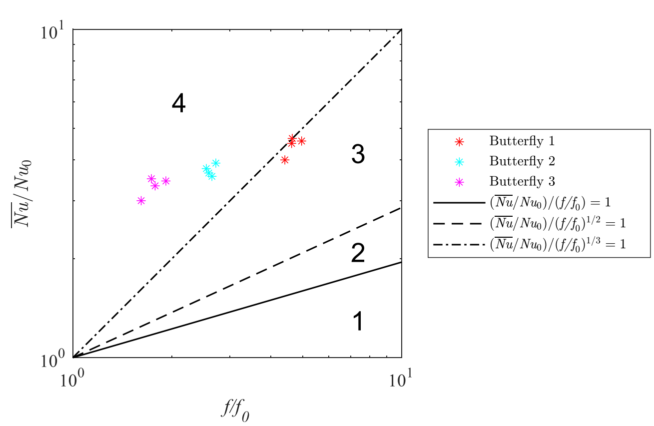

Fig. 18. Performance evluation plot for the present butterfly-shaped inserts.

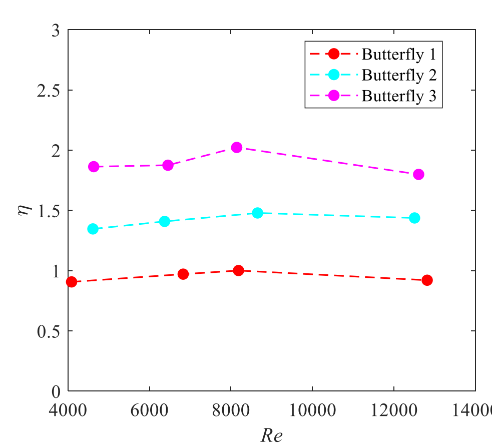

Fig. 19. Performance index as a function of the Reynolds number.

Table 6
Heat transfer enhancement solutions, obtained through AM manufacturing in heat exchangers. $\overline{Nu}$, $\overline{Nu}$ /Nu_0, and η are here referred to the best thermofluidic solution reported in each referenced work.

Heat transfer enhancement solution	Re	$\overline{Nu}$	$\overline{Nu}$ /Nu_0	η	k_i	Ref.
Heat sinks equipped with triangular fins	7056 – 28,255	190 – 475	-	-	-	[49]
Triply periodic minimal surface (diamond)	1800 – 6400	800 – 1400	-	1.3 – 0.9	1/3	[50]
Straight duct featuring Kagome-shaped unit cells	6000 – 25,000	-	7.6 – 4.8	-	-	[51]
Triply periodic minimal surface (gyroid)	9000 – 33,400	-	6.8 – 3.5	4 – 2	-	[52]
Triply periodic minimal surface (Fischer-Koch)	400 – 8000	10 – 70	-	-	-	[53]
Rough, unpolished surface – direct metal laser sintering	7500 – 30,000	-	2.4 – 1.25	-	-	[54]
Triply periodic minimal surface (special-shaped)	2000 - 9000	140 – 220	-	-	-	[55]
Present work	4000 – 14,000	150 – 440	3.5 – 4.4	1.8	1	-

gradients along the samples, allowing a clear identification of local thermofluidic effects of the adopted inserts. Three butterfly inserts presenting as swirled configuration were considered, namely Butterfly 1 (full insert), Butterfly 2 (insert with small and inclined holes), and Butterfly 3 (fully drilled insert). The test rig consisted in a pipeline through which cold water was circulated. Heat was dissipated in part of the sample by means of Joule effect. The inlet and outlet water temperatures were monitored by thermocouples. The fluid pressure was measured by adopting water column gauges upstream and downstream the inserts. The outer wall temperature was instead acquired through infrared thermography to provide a complete dataset for the estimation of useful thermofluidic quantities, such as the local and average Nusselt numbers, and the friction coefficient K related to local pressure losses. The experimental approach was validated by verifying uniform heat dissipation in the additive manufactured samples, closed energy balance for the fluid flow, and robust pressure drops measurements. The heat transfer augmentation provided by the samples investigated was finally compared with induced pressure drops by means of the performance index. The main outcomes of the present study are listed below as follows:

- The outer wall temperature is strongly affected by the type of adopted insert and its location in the tube. In fact, Butterfly 1 presented warmer wall spots downstream due to fluid stagnation, while the presence of holes in Butterfly 2 and Butterfly 3 allowed for better fluid flow behind the inserts. However, Butterfly 1 could induce higher fluid accelerations, resulting in colder wall areas far from the insert wings locations.
- The location of maximum local Nusselt number was influenced by the type of insert. In fact, the presence of divergent holes in Butterfly 2 could move to lower axial coordinates the location of Nu peaks, hence anticipating the heat transfer augmentation effect of the insert. The maximum local Nu peak of 716 was reached for Butterfly 1 at $Re = 12{,}818$.
- Butterfly 1 provided the highest average Nusselt number $\overline{Nu}$ within the observation window, for all the considered Reynolds numbers. This was due to higher flow disturbances promoted by such geometry, which hence ensured strong boundary layers disruption. The maximum Nusselt number increment was observed to be equal to about 400 % of the one reached for the plain tube geometry in the fully developed case. Moreover, the flow direction through Butterfly 2 (resulting in divergent or convergent holes) did not significantly affect the overall heat transfer, probably due to the turbulent nature of the analyzed flow.
- The average Nusselt number within the test section was found to be correlated, at least from a preliminary standpoint, with the Reynolds number and the geometrical characteristics γ through the correlation $\overline{Nu}/Pr^{0.4} = 0.06\,\gamma^{0.86}Re^{0.92}$.
- The K coefficients, through which the butterfly inserts were characterized in terms of local pressure drops, were found to be equal to 15.6, 9.6 and 4.9 for Butterfly 1, Butterfly 2 and Butterfly 3, respectively.
- Performance evaluation plots highlighted the lower energy-saving capability of Butterfly 1 with respect to its holed counterparts. The performance index at identical flow rate was estimated as almost asymptotical with the Reynolds number, and equal to about 1.9 and 1.4 for Butterfly 3 and Butterfly 2, respectively.

In conclusion, despite lower heat transfer augmentation with respect to other insert solutions, Butterfly 3 could be considered as a viable applicative option, especially for those cases where pressure drops mitigation is required. The present analysis gave in-depth insights into the thermofluidic features of additive manufactured samples for heat transfer enhancement. The assessment of local quantities related to the modified inner convection provided crucial pieces of information, which could be adopted as reference when integration of multiple additive manufactured samples or in-series inserts is needed for complex heat transfer systems. Moreover, the results shown suggest possible design strategies that can be adopted during further optimization of the heat transfer augmentation solutions. From an industrial perspective, AM tubular samples could be integrated into tube bundle modules of large-scale shell-and-tube heat exchangers or double/triple-tube heat exchangers. Connections could be therefore achieved by means of joints or quick-release flanges, which would increase the effectiveness and maintenance of heat exchangers at the expense of higher manufacturing costs. In future developments of the work, laminar flows will be investigated to achieve a comprehensive evaluation of the effects of the samples provided on the overall thermo-fluid dynamics. Possible additional developments may include changes in manufacturing material, which could enhance the overall heat transfer to the fluid. Numerical investigations on the presented inserts may disclose additional features of the local flow dynamics, hence allowing a comprehensive understanding of thermal and hydrodynamic mechanisms.

CRediT authorship contribution statement

Luca Pagliarini: Writing – original draft, Validation, Software, Methodology, Investigation, Formal analysis, Data curation, Conceptualization. **Umberto Neviani:** Writing – review & editing, Visualization, Validation, Software, Investigation, Data curation. **Teresa Primo:** Writing – original draft, Resources, Investigation, Formal analysis. **Antonio Del Prete:** Writing – review & editing, Supervision, Project administration, Funding acquisition. **Sara Rainieri:** Writing – review & editing, Supervision, Resources, Project administration, Funding acquisition.

Declaration of competing interest

We wish to confirm that there are no known conflicts of interest associated with this publication and there has been no significant financial support for this work that could have influenced its outcome.

Acknowledgments

The Authors would like to acknowledge financial support from

PNRR-M4C2- I1.1 – MUR Call for proposals n.104 of 02-02-2022 - PRIN 2022 - ERC sector PE8- Project title: MOOD4HEX - MOrphology Optimized Design for Heat EXchangers - Project Code 2022SJP2A5 - CUP Code D53D23004040006 - Funded by the European Union – NextGenerationEU. The Authors also thank the HB-Technology company of Taranto (Italy) for their invaluable support in the 3D printing of the specimens used in this study. Their expertise and technical assistance were essential for the successful fabrication of the components.

References

[1] N. Nyangchak, Emerging green industry toward net-zero economy: A systematic review, J. Clean. Prod. 378 (2022) 134622, https://doi.org/10.1016/j.jclepro.2022.134622.
[2] P. Tripathy, P.K. Jena, B.R. Mishra, Systematic literature review and bibliometric analysis of energy efficiency, Renew. Sustain. Energy Rev. 200 (2024) 114583, https://doi.org/10.1016/j.rser.2024.114583.
[3] M. Patterson, P. Singh, H. Cho, The current state of the industrial energy assessment and its impacts on the manufacturing industry, Energy Rep. 8 (2022) 7297–7311, https://doi.org/10.1016/j.egyr.2022.05.242.
[4] S. Bhattacharyya, D.K. Vishwakarma, A. Srinivasan, M.K. Soni, V. Goel, M. Sharifpur, M.H. Ahmadi, A. Issakhov, J. Meyer, Thermal performance enhancement in heat exchangers using active and passive techniques: a detailed review, J. Therm. Anal. Calorim. 147 (2022) 9229–9281, https://doi.org/10.1007/s10973-021-11168-5.
[5] N.M. Maleki, S. Pourahmad, E. Tavousi, N. Perera, P. Talebizadehsardari, A. Keshmiri, Thermal-frictional behavior of solid magnetic strip turbulator and helical coiled wire turbulator inside a double tube heat exchanger, Int. Commun. Heat Mass Transf. 161 (2025) 108406, https://doi.org/10.1016/j.icheatmasstransfer.2024.108406.
[6] M.H. Mousa, N. Miljkovic, K. Nawaz, Review of heat transfer enhancement techniques for single phase flows, Renew. Sustain. Energy Rev. 137 (2021) 110566, https://doi.org/10.1016/j.rser.2020.110566.
[7] J. Wang, C. Li, L. Zeng, T. Fu, K. Liu, Thermal performance analysis of a heat exchanger with a novel turbulator insert by using machine learning method, Case Stud. Therm. Eng. 72 (2025) 106412, https://doi.org/10.1016/j.csite.2025.106412.
[8] Y.H. Assaf, A. Akroot, K. Alnamasi, M.A. Ismail, Investigation of heat transfer performance in heat exchangers using hybrid nanofluids and twisted tape inserts with fixed special rings, Sci. Rep. 15 (2025) 18450, https://doi.org/10.1038/s41598-025-02135-3.
[9] S. Banihashemi, M. Assari, S. Javadi, S. Vahidifar, Study the effect of innovative active and passive methods on thermal characteristics and turbulent flow behaviour in a heat exchanger pipe, J. Therm. Anal. Calorim. 149 (2024) 777–797, https://doi.org/10.1007/s10973-023-12728-7.
[10] B. Mei, A.M. Abed, P. Patel, A. Kulshreshta, H. Ayed, A. Mouldi, I. Mahariq, A numerical investigation for heat transfer enhancement possibility for a novel perforated twisted hyperbolic turbulator (PTHT) inside a heated tube, Case Stud. Therm. Eng. 65 (2025) 105666, https://doi.org/10.1016/j.csite.2024.105666.
[11] B. Mei, A.M. Abed, P. Patel, A. Kedia, H. Ayed, A. Mouldi, I. Mahariq, Numerical investigation on thermal-fractional characteristics inside a heated tube enhanced with a novel grooved cone turbulator, Case Stud. Therm. Eng. 66 (2025) 105712, https://doi.org/10.1016/j.csite.2024.105712.
[12] T. Adibi, N.M. Maleki, E. Tavousi, A. Keshmiri, Enhancing the heat transfer efficiency in heated tube with a novel multi-twisted blade turbulators: A numerical analysis, Int. Commun. Heat Mass Transf. 169 (2025) 109717, https://doi.org/10.1016/j.icheatmasstransfer.2025.109717.
[13] H. Wang, Q.R. Al-amir, D.J. Jasim, H. Ayed, A. Mouldi, A. Deifalla, I. Mahariq, Enhancing the heat transfer efficiency of an engine heat exchanger through the utilization of an innovative conical braided wire turbulator, Case Stud. Therm. Eng. 61 (2024) 104873, https://doi.org/10.1016/j.csite.2024.104873.
[14] H. Wang, A.M. Abed, P. Patel, N. Patil, H. Ayed, A. Mouldi, I. Mahariq, Heat transfer enhancement inside a constant temperature pipe via clockwise and counter-clockwise twisted triangle turbulators, applicable in IC engine system, Case Stud. Therm. Eng. 65 (2025) 105672, https://doi.org/10.1016/j.csite.2024.105672.
[15] R. Pandey, U. Madanan, Heat transfer enhancement through pitch ratio optimization of butterfly inserts in minichannel heat sinks, Therm. Sci. Eng. Prog. 46 (2023) 102262, https://doi.org/10.1016/j.tsep.2023.102262.
[16] F. Bozzoli, L. Cattani, A. Mocerino, S. Rainieri, I. Tougri, M.J. Colaço, Characterisation of the heat transfer in displaced enhancement devices by means of inverse problem approach applied to IR images, Quant. Infrared Thermogr. J. 18 (2021) 108–126, https://doi.org/10.1080/17686733.2019.1700696.
[17] A. Azari, M. Derakhshandeh, An experimental comparison of convective heat transfer and friction factor of Al2O3 nanofluids in a tube with and without butterfly tube inserts, J. Taiwan Inst. Chem. Eng. 52 (2015) 31–39, https://doi.org/10.1016/j.jtice.2015.02.009.
[18] L. Pagliarini, F. Bozzoli, L. Cattani, S. Rainieri, Morphological optimization of butterfly-shaped inserts for heat transfer enhancement in tubular heat exchangers: a numerical study, J. Phys. Conf. Ser 2766 (2024) 012185, https://doi.org/10.1088/1742-6596/2766/1/012185.
[19] L. Cattani, B. Fabio, S. Rainieri, Inverse problem approach applied to the study of heat transfer maximization: shape optimization of butterfly inserts, Heat Transf. Eng. 45 (2024) 1117–1127, https://doi.org/10.1080/01457632.2023.2241179.
[20] V. Deshmukh, R.M. Sarviya, Categorical review of experimental and numerical studies on twist tape inserts in the single-phase flow tubular heat exchanger, J. Therm. Anal. Calorim. 149 (2024) 2985–3025, https://doi.org/10.1007/s10973-024-12886-2.
[21] L. Zhou, J. Miller, J. Vezza, M. Mayster, M. Raffay, Q. Justice, Z. Al Tamimi, G. Hansotte, L.D. Sunkara, J. Bernat, Additive Manufacturing: A comprehensive review, Sensors 24 (2024), https://doi.org/10.3390/s24092668.
[22] I. Kaur, P. Singh, State-of-the-art in heat exchanger additive manufacturing, Int. J. Heat Mass Transf. 178 (2021) 121600, https://doi.org/10.1016/j.ijheatmasstransfer.2021.121600.
[23] M. Ali, A. Ul-Hamid, L.M. Alhems, A. Saeed, Review of common failures in heat exchangers – Part I: mechanical and elevated temperature failures, Eng. Fail. Anal. 109 (2020) 104396, https://doi.org/10.1016/j.engfailanal.2020.104396.
[24] F. Lu, Q. Ma, E. Liu, R. Wei, J. Bai, Q. Gao, J. Qi, Advancements in understanding the microstructure and properties of additive manufacturing Ti-6Al-4V alloy: A comprehensive review, J. Alloys Compd. 1027 (2025) 180543, https://doi.org/10.1016/j.jallcom.2025.180543.
[25] M.L. Huber, E.W. Lemmon, I.H. Bell, M.O. McLinden, The NIST REFPROP database for highly accurate properties of industrially important fluids, Ind. Eng. Chem. Res. 61 (2022) 15449–15472.
[26] M.A. Salam, Fundamentals of Pneumatics and Hydraulics, Springer, 2022.
[27] S.I. Edition, 2009 ASHRAE® HANDBOOK, 2009.
[28] D.P.D. Theodore, L. Bergman, A.S. Lavine, F.P. Incropera, Fundamentals of Heat and Mass Transfer, John Wiley & Sons, 2011.
[29] M.W. Azam, L. Cattani, M. Malavasi, F. Bozzoli, Experimental study of the corrugation profile effect on the local heat transfer coefficient, energies (Basel). 16 (2023). https://doi.org/10.3390/en16207181.
[30] L. Cattani, F. Bozzoli, S. Rainieri, Inverse problem approach applied to the study of heat transfer maximization: shape optimization of butterfly inserts, Heat Transf. Eng. 45 (2024) 1117–1127, https://doi.org/10.1080/01457632.2023.2241179.
[31] S.J. Kline, Describing uncertainties in single-sample experiments, Mech. Eng. 75 (1953) 3–8.
[32] J.T. Cieśliński, S. Smolen, D. Sawicka, Free convection heat transfer from horizontal cylinders, Energies (2021) 14, https://doi.org/10.3390/en14030559.
[33] S. Kakaç, R.K. Shah, W.T. Aung, Handbook of single-phase convective heat transfer, 1987. https://api.semanticscholar.org/CorpusID:93232424.
[34] M. Rahimi, R. Mehryar, Numerical study of axial heat conduction effects on the local Nusselt number at the entrance and ending regions of a circular microchannel, Int. J. Therm. Sci. 59 (2012) 87–94, https://doi.org/10.1016/j.ijthermalsci.2012.04.017.
[35] S.P. Mahulikar, H. Herwig, Fluid friction in incompressible laminar convection: Reynolds' analogy revisited for variable fluid properties, Eur. Phys. J. B. 62 (2008) 77–86, https://doi.org/10.1140/epjb/e2008-00115-0.
[36] A. Tanase, D.C. Groeneveld, An experimental investigation on the effects of flow obstacles on single phase heat transfer, Nucl. Eng. Des. 288 (2015) 195–207, https://doi.org/10.1016/j.nucengdes.2015.04.004.
[37] M. Yao, M. Nakatani, K. Suzuki, Flow visualization and heat transfer experiments in a turbulent channel flow obstructed with an inserted square rod, Int. J. Heat Fluid Flow 16 (1995) 389–397, https://doi.org/10.1016/0142-727X(95)00047-T.
[38] L. Godson, B. Raja, D. Mohan Lal, S. Wongwises, Enhancement of heat transfer using nanofluids—An overview, Renew. Sustain. Energy Rev. 14 (2010) 629–641, https://doi.org/10.1016/j.rser.2009.10.004.
[39] M.O.Garg Varun, H. Nautiyal, S. Khurana, M.K. Shukla, Heat transfer augmentation using twisted tape inserts: A review, Renew. Sustain. Energy Rev. 63 (2016) 193–225, https://doi.org/10.1016/j.rser.2016.04.051.
[40] J.F. Fan, W.K. Ding, J.F. Zhang, Y.L. He, W.Q. Tao, A performance evaluation plot of enhanced heat transfer techniques oriented for energy-saving, Int. J. Heat Mass Transf. 52 (2009) 33–44, https://doi.org/10.1016/j.ijheatmasstransfer.2008.07.006.
[41] P. Promvonge, P. Promthaisong, S. Skullong, M.E. Nakhchi, Thermal effectiveness enhancement in heat exchange tube using louver-punched V-baffles, Int. J. Heat Mass Transf. 225 (2024) 125411, https://doi.org/10.1016/j.ijheatmasstransfer.2024.125411.
[42] A.J. Modi, N.A. Kalel, M.K. Rathod, Thermal performance augmentation of fin-and-tube heat exchanger using rectangular winglet vortex generators having circular punched holes, Int. J. Heat Mass Transf. 158 (2020) 119724, https://doi.org/10.1016/j.ijheatmasstransfer.2020.119724.
[43] F. Bozzoli, L. Cattani, S. Rainieri, Cross-helix corrugation: the optimal geometry for effective food thermal processing, Int. J. Heat Mass Transf. 147 (2020) 118874, https://doi.org/10.1016/j.ijheatmasstransfer.2019.118874.
[44] S. Eiamsa-ard, P. Nivesrangsan, S. Chokphoemphun, P. Promvonge, Influence of combined non-uniform wire coil and twisted tape inserts on thermal performance characteristics, Int. Commun. Heat Mass Transf. 37 (2010) 850–856, https://doi.org/10.1016/j.icheatmasstransfer.2010.05.012.
[45] S. Eiamsa-ard, C. Thianpong, P. Eiamsa-ard, Turbulent heat transfer enhancement by counter/co-swirling flow in a tube fitted with twin twisted tapes, Exp. Therm. Fluid Sci. 34 (2010) 53–62, https://doi.org/10.1016/j.expthermflusci.2009.09.002.
[46] T. Adibi, N.M. Maleki, E. Tavousi, A. Keshmiri, Enhancing the heat transfer efficiency in heated tube with a novel multi-twisted blade turbulators: A numerical analysis, Int. Commun. Heat Mass Transf. 169 (2025) 109717, https://doi.org/10.1016/j.icheatmasstransfer.2025.109717.

[47] N.M. Maleki, T. Adibi, Assessment of heat transfer efficiency through the application of transverse waves within a double tube heat exchanger, Int. Commun. Heat Mass Transf. 166 (2025) 109175, https://doi.org/10.1016/j.icheatmasstransfer.2025.109175.

[48] S. Kakaç, A.E. Bergles, F. Mayinger, H. Yüncü, Heat Transfer Enhancement of Heat Exchangers, Springer Science & Business Media, 2013.

[49] A. Alimehr, A. Nikniazi, A. Jalali, M.R. Daymond, M. Pahlevani, V. Fallah, Heat sink design investigation via CFD thermal analysis and additive manufacturing rapid prototyping, Int. J. Adv. Manuf. Technol. 141 (2025) 4473–4487, https://doi.org/10.1007/s00170-025-16932-7.

[50] X. Yang, Y. Yang, B. Liu, X. Chen, Z. Kuai, Y. Zhang, Y. Gao, Z. Li, R. Wang, Y. Li, Q. Zhang, Vorticity-driven heat transfer and thermo–hydraulic trade-offs in selective-laser-melted CuCrZr minimal-surface heat exchangers, Appl. Therm. Eng. 287 (2026) 129473, https://doi.org/10.1016/j.applthermaleng.2025.129473.

[51] Y. Aider, P. Singh, K. Nithyanandam, Experimental and numerical study on conjugate heat transfer in additively manufactured straight duct featuring Kagome-shaped unit cells, Appl. Therm. Eng. 280 (2025) 128565, https://doi.org/10.1016/j.applthermaleng.2025.128565.

[52] C. Xu, Y. Rao, K. Yeranee, Experiments and numerical analysis of turbulent flow heat transfer and pressure loss of a channel with triply periodic minimal surface structures, Int. J. Therm. Sci. 220 (2026) 110334, https://doi.org/10.1016/j.ijthermalsci.2025.110334.

[53] J. Wang, C. Qian, B. Yu, F. Zhang, R. Ma, J. Shi, J. Chen, Design and optimization of additive manufactured Fischer-Koch-structured heat exchanger for enhanced heat transfer efficiency, Int. Commun. Heat Mass Transf. 159 (2024) 108078, https://doi.org/10.1016/j.icheatmasstransfer.2024.108078.

[54] L.M. Wright, J. Liu, B. Kamrath, M.C. Morris, Evaluation of additively manufactured heat exchanger tubes using experimental and conjugate heat transfer analysis. Turbo Expo: Power for Land, Sea, and Air, American Society of Mechanical Engineers, 2023. V07BT13A016.

[55] Y. Zhang, F. Peng, H. Jia, Z. Zhao, P. Wang, S. Duan, H. Lei, Conformal geometric design and additive manufacturing for special-shaped TPMS heat exchangers, Int. J. Heat Mass Transf. 247 (2025) 127146, https://doi.org/10.1016/j.ijheatmasstransfer.2025.127146.